TECHNISCHE UNIVERSITÄT WIEN
Vienna | Austria

DIPLOMARBEIT

Electrochemical Surface Investigations of TiO_2 Rutile(110)

Ausgeführt am Institut für Angewandte Physik
der Technischen Universität Wien

Unter Anleitung von Univ.Prof. Dr.techn. Ulrike Diebold
und Univ.Ass. Dr. Stijn Mertens

durch

Iris Dorner

Argentinierstrasse 16/3/42 1040 Wien

Contents

Abstract

Electrochemical surface science aims to study surfaces under ambient atmosphere and electrochemical conditions, which approach those relevant for applications more closely than ultrahigh vacuum. While this branch of surface science has gained momentum for noble metal samples, oxides have so far rarely been studied.

In this thesis, several improvements have been made to our electrochemical scanning tunnelling (EC-STM) methodology, which is one of the main techniques in electrochemical surface science. Platinum iridium tips were implemented, since the more widely used tungsten tips were found to be unstable in aqueous electrolyte and thus contaminate the surface. A palladium-hydrogen reference electrode was developed to replace unreliable quasi-reference electrodes, improving electrochemical potential control and imaging conditions. Oxygen removal in an environmental chamber was optimised, impeding the reactions it induces and the resulting artefacts.

The resulting technical improvements were put to the test by studying the rutile TiO_2(110), an important (photo-)catalyst and robust oxide model system. For the unmodified surface in electrolyte, atomic resolution was obtained, and the appearance in EC-STM was compared to well-known studies in vacuum. Also modification of the rutile TiO_2(110) surface by adsorption of benzoic acid and grafting of aryl radicals were investigated. While the presented *in situ* studies on rutile TiO_2(110) are not yet plentiful, the methodological improvements are expected to allow accelerated progress in future.

Elektrochemische Oberflächenmessungen auf TiO_2 Rutil(110)

Zusammenfassung

Die elektrochemische Oberflächenphysik untersucht Oberflächen unter Bedingungen, welche der Umgebung in technologischen Anwendungen ähnlicher ist als dem in der Oberflächenphysik normalerweise üblichen Ultrahochvakuum. Während dieser Zweig der Oberflächenphysik für Edelmetallproben bereits Fahrt aufgenommen hat, gibt es bis dato wenig Untersuchungen an Oxiden.

Im Zuge dieser Diplomarbeit wurden mehrere Verbesserungen an einem elektrochemischen Rastertunnelmikroskop (EC-STM) eingeführt, welches eines der wichtigsten Werkzeuge der elektrochemischen Oberflächenphysik ist. Die Verwendung von Platin-Iridiumspitzen wurde implementiert, da sich die weithin genutzten Wolframspitzen in wässrigem Elektrolyt als instabil herausstellten und die untersuchte Oberfläche kontaminierten. Eine Palladium-Wasserstoffreferenzelektrode wurde konstruiert und charakterisiert um unverlässliche Quasireferenzelektroden zu ersetzen, wodurch Potentialkontrolle und Bildgebung verbessert wurden. Sauerstoffentfernung durch Ersetzen der Umgebungsluft wurde optimiert, um sauerstoffinduzierte Prozesse und die daraus resultierenden Artefakte zu unterdrücken.

Diese technischen Verbesserungen wurden für die Untersuchung von Rutil TiO_2(110) ausgenutzt, ein wichtiger (Photo-)Katalysator sowie robustes Modellsystem für die Untersuchung von Oxiden. Auf der unmodifizierten Oberfläche wurde atomare Auflösung erreicht, und das Erscheinungsbild in EC-STM mit Ergebnissen aus dem Ultrahochvakuum verglichen. Modifikation der Rutil TiO_2(110) Oberfläche durch Adsorption von Benzoesäure oder Arylradikalen wurde untersucht. Obwohl die präsentierten *in situ* Untersuchungen auf Rutil TiO_2(110) noch keine wissenschaftlichen Aussagen zulassen, sollten die methodologischen Verbesserungen für weitergehende Messungen wertvoll sein.

Acknowledgements

First of all, I would like to express my gratitude and appreciation to my supervisors, Ulrike Diebold and Stijn Mertens, for giving me the chance to work on such an interesting topic, for enabling me to do so, and for providing this prosperous and encouraging environment. Further thanks go to Matthias Müllner, for sharing his experience and expertise with me. I also feel grateful to Michael Schmid, always happy to teach me more physics, and Jan Balajka, for the assistance with troubleshooting. I would like to thank the whole of Ulrike Diebold's group, for the stimulating conversations, and for sharing so much knowledge with me.

Finally, I would like to thank my family, for everything, and for supporting my physics studies.

1 Introduction

The increasingly pressing need for sustainable energy production and storage as well as environment-friendly and CO_2-neutral chemical processes has been met with increased interest in surface science studies under technologically relevant conditions. While surface science under such conditions has been practised for several decades [1] [2], it has been limited to the study of noble metals, for the methodology to take on more complex systems was not available. For technological applications, the cost and availability of the materials used is an important factor, making earth-abundant metal oxides the prime candidates to replace noble metal catalysts. Electrochemical surface science of oxide materials is therefore very timely, and requires further development of existing methodologies.

TiO_2 is an important heterogeneous catalyst, photo-catalyst, and electrode in solar cells [3] [4] [5]. Rutile $TiO_2(110)$ is a robust and well-characterized surface [3], and therefore an excellent system for method development in electrochemical surface science.

TiO_2 crystallizes in several structures, the most stable and most widely studied of which is rutile. It is a tetragonal crystal (a = b = 4.584 Å, c = 2.953 Å) with a titanium atom in the center of an elongated octahedron of oxygen atoms, the unit cell is shown in figure 1.1 [3]. As many surface science techniques, and in particular STM, require good electrical conductivity, the limited conductance of this wide band gap (3.0 eV [6]) semiconductor can be increased by doping, for instance with niobium, or by introducing oxygen vacancies by reduction [7].

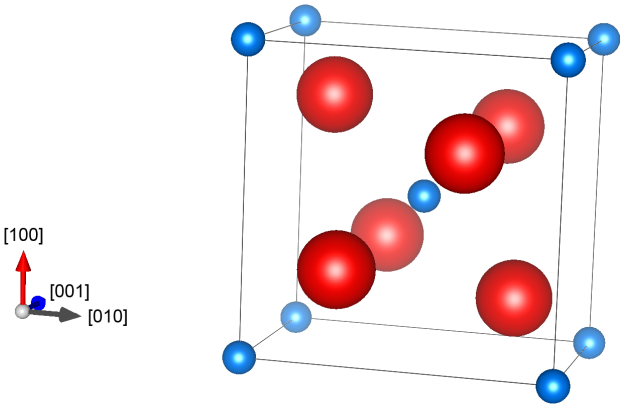

Figure 1.1: Model of the rutile TiO_2 unit cell. Titanium in blue, oxygen in red.

The (110) face of rutile is shown in figure 1.2. This surface is composed of rows of fivefold coordinated Ti atoms, flanked by threefold coordinated in-plane O atoms, and sixfold coordinated Ti atoms under bridging O atoms. [3].

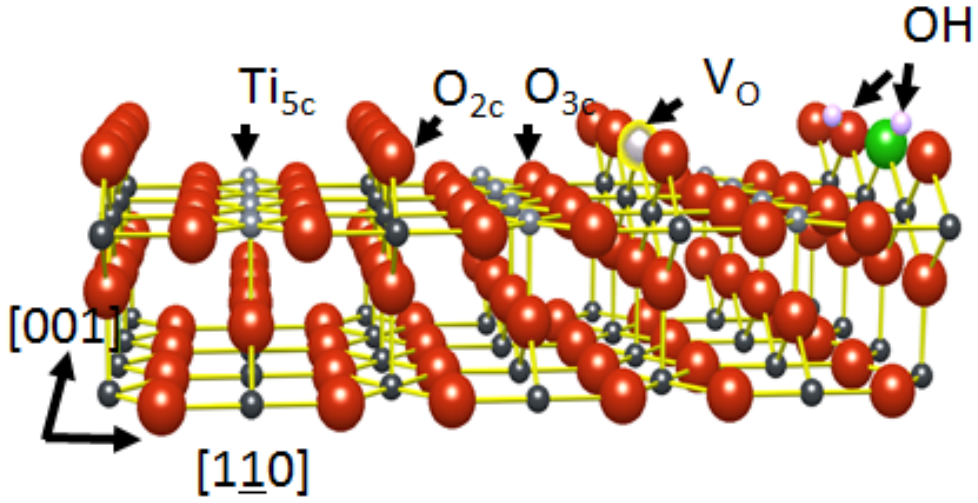

Figure 1.2: Model of the rutile TiO_2(110) surface, taken from [8]. Titanium in grey, oxygen in red. Oxygen vacancies (V_O) and surface OH-groups are also shown as examples for common surface defects.

2 Techniques

2.1 Scanning Tunnelling Microscopy

Scanning tunnelling microscopy (STM, also short for scanning tunnelling microscope) is based on the quantum mechanical interaction between a pointed probe and the sample. Quantum tunnelling allows particles to pass a barrier which classically they would not be able to surmount. Application of a bias voltage between tip and substrate, although not in contact, leads to a measurable electric current.

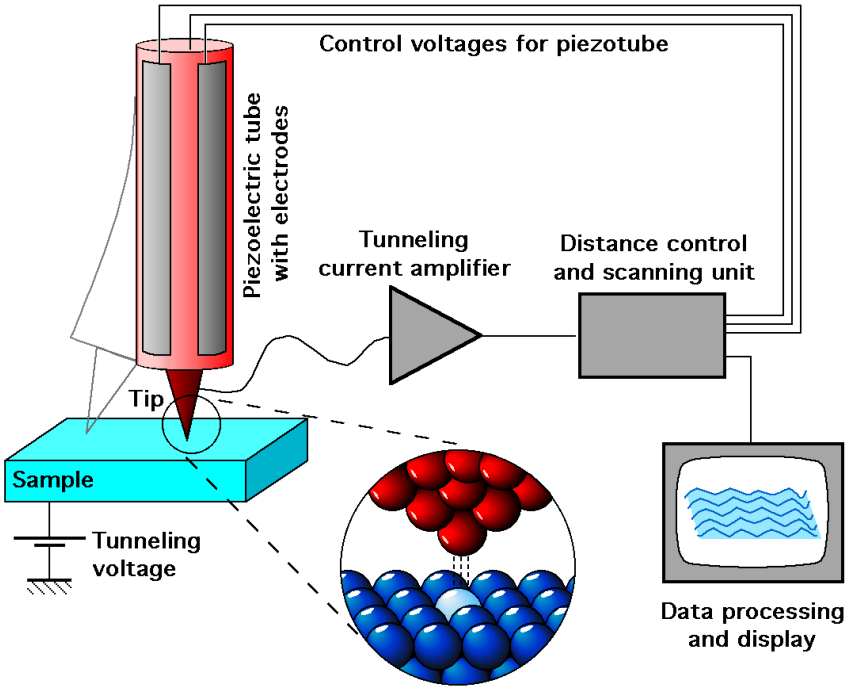

Figure 2.1: Schematic diagram of a scanning tunnelling microscope. Image © Michael Schmid

For a basic treatment of quantum tunneling current we consider a rectangular potential barrier separating the conductive probe and sample. The particle-wave duality allows the electrons to pass the barrier. The transmission T is proportional to the squared modulus of the wave function passing the barrier, which we can calculate from the Schrödinger equation

$$(-\frac{\hbar^2}{2m}\nabla^2 + V)\Psi = E\Psi.$$

We consider only electrons close to the Fermi level and assume equal work functions of tip and sample, so the work function equals the height of the barrier ϕ. After passing a barrier with width d, we obtain the transmission:

$$T \propto |\Psi(d)|^2 \propto e^{-2\sqrt{\frac{2m\phi}{\hbar^2}}d}.$$

As the tunnelling current is proportional to this transmission, there is an exponential decay of electrical current with an increasing potential barrier width d.

Scanning tunnelling microscopes are mostly operated in constant current mode. In this mode, the distance between probe and sample is adjusted to maintain constant tunnelling current via a feedback loop, while the probe is scanned over the sample line by line, creating a map of the sample's surface. The map shows the electronic density of states, which allows for conclusions about the location of single atoms, as well as their electronic state, among other information.

The lateral resolution of STM is limited by the distance d between probe and sample, the radius of the probe, and the corrugation of the sample. Lowering the distance allows for better resolution, but also causes stronger interaction between probe and sample, which may lead to artefacts such as atom manipulation by the tip. The radius of the probe ideally equals the radius of one atom of the probe material, which is usually tungsten or a platinum-iridium alloy. Also, the probe tips must be very pointed, as the STM image will otherwise reflect tip rather than sample structure. Preparing a clean and suitably shaped probe is therefore one of the the main technical challenges that STM presents.

Another challenge in STM are vibrations from the outside. These may lower the resolution, cause imaging artefacts or cause the probe to crash into the sample. Suspending the STM by springs or levitating it magnetically is therefore required.

To be able to scan the sample, either probe or sample must be moved. In the setups used here, and shown schematically in figure 2.1, the sample remains static, and the probe is moved by a piezoelectric tube as this provides both good stability in z- direction and flexibility in x and y-direction. The

piezoelectric tube also allows precise movement in the sub-angstrom range [9].

The STM images shown in this thesis were optimized by removing a background fit (piezo creep or line by line), and in some images bad lines were replaced with a fit to the neighbouring lines or a nonlinear undistort was applied, as described in [10].

2.2 Electrochemical STM

Scanning tunnelling microscopy under electrochemical potential control (*in situ* or electrochemical STM, EC-STM) employs the principle described in section 2.1 while keeping sample and tip in electrolyte. The potentials of sample and tip are controlled independently relative to a known reference potential, by means of a bipotentiostat. Figure 2.2 shows a schematic of the system. A counter electrode carries any net electrochemical current through the sample [2].

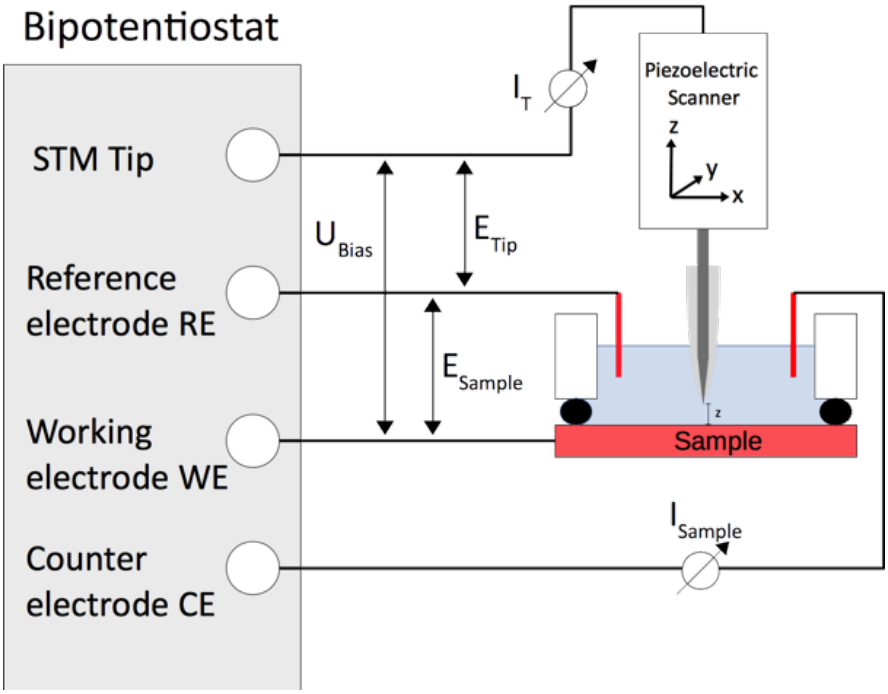

Figure 2.2: Schematic diagram of an EC-STM.
Image ©Matthias Müllner

The electrolyte is contained in a cell designed specifically for use in the EC-

STM, a cylindrical compartment made from polychlorotrifluoroethene that is pressed onto the sample with springs. Figure 2.3 shows the setup as seen from the top, through the opening that accommodates the STM scanner. The sample plate, carrying sample and cell, is suspended in a glass environmental chamber purged with purified argon, to allow measurements in an oxygen-poor atmosphere.

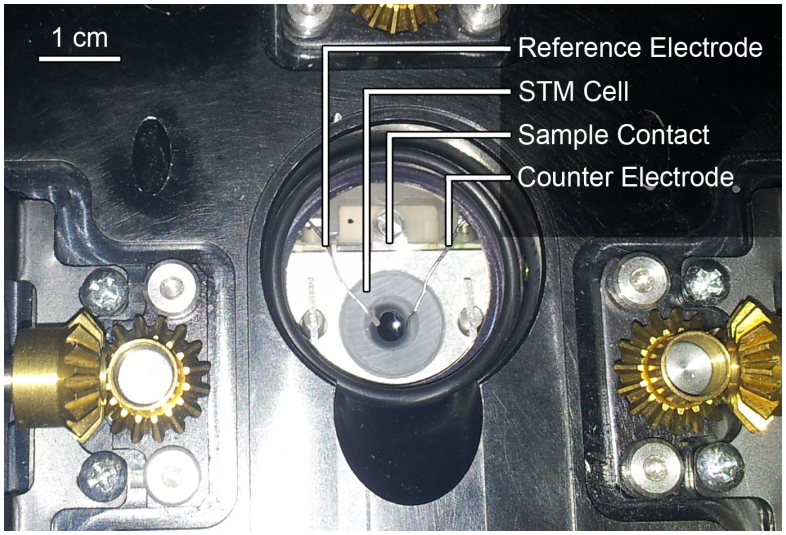

Figure 2.3: Top view of EC-STM cell and electrodes

2.3 Atomic Force Microscopy

Atomic Force Microscopy (AFM), another scanning probe technique, measures the repulsive or attractive interaction between a small, pointed probe on a cantilever and the sample.

The forces accessible by AFM include repulsion forces due to Pauli exclusion, chemical binding forces, van-der-Waals-forces, electrostatic forces, magnetic forces, friction, hydrophilic/hydrophobic forces and capillary forces. Not all of them necessarily influence a given measurement. Pauli exclusion and chemical binding forces are relevant over shorter ranges than van-der-Waals and electrostatic forces, magnetic interaction can only be measured with a suitable tip, and hydrophilic or hydrophobic forces and capillary forces are relevant only in the presence of liquids.

The sharp probe is placed on the end of a cantilever, which bends due to the

interaction with the sample. This bending is measured, usually by laser beam deflection or interferometry. Other options are measuring the capacitance between the cantilever and a static plate, or the bending of the cantilever with piezoelectric sensors. Imaging modes for AFM are contact and non-contact AFM, and tapping mode as an intermediate. For contact AFM, the tip is kept in direct contact with the sample. Either the bending of the cantilever or the feedback required to keep the bending constant can be recorded as topography. For non-contact AFM, the cantilever oscillates with a frequency close to its resonance frequency. The resonance frequency shifts due to the forces between tip and sample, and this frequency shift can be used as feedback analogously to the tunnelling current for STM. In tapping mode, the cantilever is driven to oscillate while in intermittent contact with the surface, and the change of amplitude while making contact with the surface is used as feedback. For the AFM measurements presented here, non-contact mode AFM with silicon tips, silicon cantilevers (resonance frequency 64.8-90.0 kHz, spring constant 0.6-3.5 N/m) and laser beam deflection were used.

2.4 Electrochemical Methods

Voltammetry measures the response of an electrochemical system to the perturbation resulting from an applied potential. Potentials are applied to the working electrode, relative to a known potential provided by the reference electrode. Resulting currents from redox processes and capacitive processes at the working electrode are carried by a counter electrode, to avoid disturbing the equilibrium underlying the stable potential of the reference electrode. In case of potentiometry, no potentials or currents are applied, and the potential is measured over time.

The redox process can be written as $Ox + ne^- \rightleftharpoons Red$, the oxidized species accepts n electrons to form the reduced species, or vice versa. Whether a given process can take place at the applied potential is governed by the Nernst equation

$$E = E^0 + \frac{RT}{nF} ln \frac{a_{Ox}}{a_{Red}} \tag{2.1}$$

which is derived by minimizing the Gibbs free energy, and thus reflects thermodynamic properties. E^0 is the standard reduction potential, R the gas constant, F the Faraday constant, or the number of Coulombs per mole of electrons, and a denominates the activity of the reactant, which at low concentrations can be approximated with the concentration.

In potentiometric experiments, no potential or current is applied which could drive a reaction, so thermodynamic description is sufficient for many systems. In voltammetric experiments, on the other hand, thermodynamic properties are measured superimposed with kinetic properties of the system. Kinetic factors affecting the measurements shown in this thesis are transport and electrode area. The latter can be removed from experimental results by showing current densities instead of currents. Transport of reactant to and product away from the electrode surface can take place via diffusion, convection or migration. Migration is limited by the magnitude of the electric field, and is suppressed by adding sufficient background electrolyte. Convection effects are negligible for short measuring times in unstirred solutions. Voltammograms show both faradaic currents, those responsible for redox reactions taking place, and non-faradaic currents, attributed to charging the electrochemical double layer on the electrode.

Potentials can only be measured relative to each other. In order to be able to give absolute information, potentials are measured relative to electrodes at a known potential, called reference electrodes (REs). They can then be represented against any other RE by adding the difference between the potential of the used RE and the desired RE, $E_{\text{vs RE1}} = E_{\text{vs RE2}} + (E_{RE1} - E_{RE2})$. Potentials shown here are represented against the standard hydrogen electrode (SHE), the accepted standard in electrochemistry for E=0 V.

2.5 Ultrahigh Vacuum Systems

The sample was also treated and STM performed on it in ultrahigh vacuum (UHV). This allows for convincing comparison to results obtained in UHV, which to this date are more abundant in oxide surface science than results obtained at ambient pressure. It also allows for reduction of TiO_2 in order to make it conductive.

Ultrahigh vacuum systems operate at a pressure between 10^{-7} mbar (1 mbar $= 10^2 \frac{kg}{m \times s^2}$) and 10^{-11} mbar. These pressures are achieved by several pumps, in our case a scroll pump, a turbomolecular pump, an ion pump and a titanium sublimation pump.

The scroll pump has a spiral translated along a circular path pressing against a metal hull, and reaches pressures up to about 10^{-3} mbar. It creates a forevacuum to supply the turbomolecular pump. The turbomolecular pump is composed mainly by a stator and a rotor, which rotates with velocities close

to the average velocity of the gas molecules, between 100 and 1000 m/s. Collisions between the gas molecules and the pump's rotor or stator give them an impulse towards the prevacuum chamber, creating pressures down to 10^{-11} mbar. The ion pump ionizes gas molecules by collisions with electrons or with previously ionized molecules, accelerates them in an electric field, and implants them into a metal, in our case titanium, which has the additional benefit of binding reactive gases. This quality of titanium is also used by the titanium sublimation pump. Electric current heats a titanium wire, causing the titanium to sublimate. The titanium gas condensates on the cooled surface around the wire and everywhere within line of sight, forming a highly reactive layer to bind residual gases.

The pressure that can be reached by pumping limited several factors, mainly adsorbates inside the chamber and outgassing of the material itsself. The time both processes take and target pressure cannot be reached is heavily reduced by baking the vacuum chamber after closing it, which means heating it to between 150 and 250°C for several days while running the fore-vacuum and the turbomolecular pump.

2.6 Experimental Details

To achieve a clean and flat surface with as few unwanted adsorbates as possible, and a well defined state to start each measurement from, TiO_2 samples are immersed in alkaline piranha, composed of 3/4 NH_4 and 1/4 H_2O_2, heated to 65 °C and stirred for 10 minutes. After rinsing with water, they are sonicated in water for another 10 minutes. The alkaline piranha etches contaminants on the surface, as well as the surface itself, to yield clean samples with large terraces [11]. The sonication removes any remnants of contamination or piranha solution on the surface.
Au samples are flame annealed for several minutes and then cooled under glass in air.
Pd wires are flame annealed for one minute and cooled in air inside the glass cell.

Sample preparation in UHV involves various cycles of sputtering and annealing. The sample was sputtered with Ar gas at a chamber pressure of 1 $\times$ 10^{-6} mbar, at 1keV, for about 5 minutes. Then it was annealed to 710 °C via resistive heating. This is also the procedure employed to make a new TiO_2 sample conductive.

EC-STM and AFM were performed with an Agilent 5500 AFM/STM with built-in bipotentiostat. Cyclic voltammetry and chronopotentiommetry were performed using a Metrohm-Autolab PGSTAT32 potentiostat/galvanostat, in a standard two-compartment glass cell carrying a Ag/AgCl/3M NaCl reference electrode and Pt wire counter electrode. Ultrapure water (resistivity 18.2 MΩcm, total organic carbon $\leq$ 3 ppb, MilliQ, Millipore) was used throughout. All glassware as well as the STM cell and counter electrode were boiled in 20% nitric acid and rinsed in water before measurements. The rutile TiO_2 samples were purchased from SurfaceNet GmbH, Au(111) samples from Mateck. The palladium wire was obtained from Goodfellow Cambridge Ltd (diameter 0.5 mm, purity 99.95 %, as drawn), the platinum-iridium wire from Advent Research Materials Ltd (80% Pt 20% Ir, diameter 0.25 mm, temper hard, purity 99.98%). Electrolytes were prepared from 70% perchloric acid, 30% hydrochloric acid (both Merck suprapur), 95-97% sulfuric acid, 30% hydrogen peroxide, 25% ammonia solution (all three Merck emsure, analysis grade), sodium sulfate (Amresco, ACS grade), sodium hydroxide (Sigma-Aldrich), 3,5-bis-tert-butylaniline (Tokyo Chemical Industry Co. Ltd, purity 98.0%), sodium nitrite, benzoic acid (both Sigma-Aldrich, ACS grade, purity 99%), or sodium phosphate (Sigma Aldrich, purity 99%).

3 Palladium-Hydrogen Reference Electrode

3.1 Theoretical Background

A good reference electrode is an electrode that generates a stable and well-defined Nernst potential. Considering the Nernst equation (eq. 2.1), and assuming a constant temperature, this implies that the activity ratio a_{Ox}/a_{Red} must be kept constant, even if small amounts of current flow. In practice, this is often achieved by choosing redox substances that occur as pure phases, whose activities equal one. An additional important requirement is fast electron transfer kinetics, so that thermodynamic equilibrium is always maintained. A quasi-reference electrode (QRE) is an electrode for which at least one of the above criteria is not met, so that a stable and predictable reference potential is not obtained. For EC-STM, a Pt QRE consisting of a simple wire in contact with the electrolyte is often used. The electrode can be made very small and avoids the risk of contaminating the electrolyte, but comes at the expense of accuracy and stability. QREs are usually employed when the conditions prohibit the use of proper reference electrodes, for example very high temperatures or some non-aqueous solvents [12].

The dimensions of the EC-STM cell substantially limit the size of electrodes that can be used, and the reference electrode must not contaminate the sample, precluding the use of the most common reference electrodes. The palladium-hydrogen reference electrode (Pd:H) described in this chapter fulfils both criteria, it is a single metal wire and requires no ions in the electrolyte. The ability of palladium to absorb hydrogen makes it a suitable candidate for a reference electrode usable also in hydrogen-free solutions [13].

Hydrogen can dissolve in palladium, yielding a solid solution. In the resulting non-stochiometric compound PdH_x, Pd retains its fcc crystal structure, and H occupies the octahedral voids, leading to a rocksalt crystal structure at x=1. The lattice constant expands with hydrogen absorption [14].

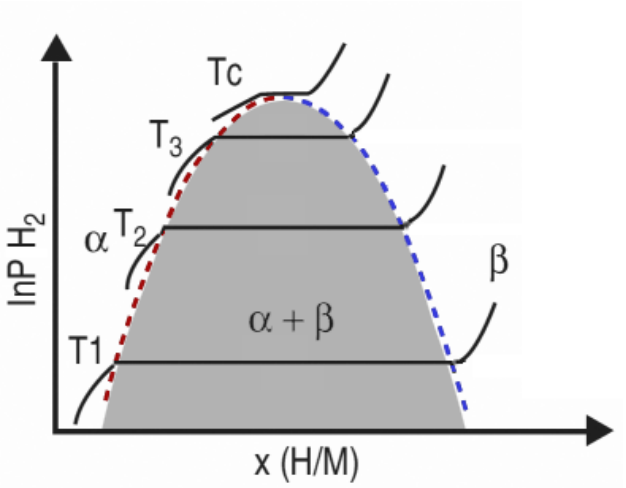

Figure 3.1: Pressure-composition-temperature diagram of PdH_x, from [15]. Dashed lines show solubility limit (red) and terminal solubility limit (blue), the grey area highlights the miscibility gap between α- and β-phase.

Figure 3.1 shows the pressure-composition-temperature diagram of PdH_x. Up to the temperature dependent solubility limit (red line), PdH_x forms the α - phase, gradually stretching the lattice constant from 0.3890 nm for pure Pd up to 0.3895 nm. Above the also temperature-dependent terminal solubility limit (blue line), the β-phase is the only crystallographic phase present and the lattice constant is further stretched to 0.4025 nm. At room temperature, the solubility limit is about x=0.05 and the terminal solubility limit is x=0.6. Between these hydrogen concentrations, the phase diagram shows a miscibility gap. In this region, both α- and β-phase are present, resulting in a saturated α-phase independent of fluctuations in hydrogen concentration [13][16][14].

The Nernst-potential-determining reaction of the Pd:H electrode is

$$H^+ + e = (Pd - H)_\alpha \tag{3.1}$$

when in the saturated α - phase, and

$$H^+ + e = \frac{1}{2}H_2 \tag{3.2}$$

when in the β - phase. The compositional region where a stable potential is expected coincides with the miscibility gap. The dominating potential is that of the saturated α-phase, and the presence of the β-phase ensures that at finite temperatures the lower-energy α-phase will always be saturated. The

resulting potential is +50 mV compared to a reversible hydrogen electrode (RHE) [16], or $E = 0.05V - 0.059V * \text{pH}$ against the standard hydrogen electrode (SHE).

Using electrochemistry shorthand, in which vertical bars indicate phase boundaries, the specific systems in which measurements for this chapter were carried out are

$$\text{Pt}|\text{Pd, Pd:H}|\text{H}_2|\text{H}^+, \text{ClO}_4^-, \text{H}_2\text{O}|\text{Na}^+, \text{Cl}^-, \text{H}_2\text{O}|\text{AgCl}|\text{Ag} \tag{3.3}$$

and

$$\text{Pt}|\text{Pd, Pd:H}|\text{H}_2|\text{H}^+, \text{Na}^+, \text{SO}_4^{2-}, \text{H}_2\text{O}|\text{Na}^+, \text{Cl}^-, \text{H}_2\text{O}|\text{AgCl}|\text{Ag} \tag{3.4}$$

for palladium-hydrogen measurements, as well as the similar systems

$$\text{Pt}|\text{H}^+, \text{ClO}_4^-, \text{H}_2\text{O}|\text{Na}^+, \text{Cl}^-, \text{H}_2\text{O}|\text{AgCl}|\text{Ag} \tag{3.5}$$

and

$$\text{Pt}|\text{H}^+, \text{Na}^+, \text{SO}_4^{2-}, \text{H}_2\text{O}|\text{Na}^+, \text{Cl}^-, \text{H}_2\text{O}|\text{AgCl}|\text{Ag} \tag{3.6}$$

for platinum measurements. The same information as in eq. 3.3 is shown in schematic 3.2, for clarity. A Pd wire, in which both Pd and Pd:H are present, is in contact with the electrolyte, H^+ and ClO_4^- ions in aqueous solution. At the other side, an Ag wire is in contact with an aqueous solution of Na^+, Cl^- and a small concentration of Ag^+ ions, in a glass compartment. For Pt measurements, the Pd wire was replaced with a Pt wire, and for regulation of pH the ions in the electrolyte were substituted. The electrolyte 0.1 M HClO_4 was chosen because it is frequently used in EC-STM measurements. The ClO_4^- ions were substituted with SO_4^{2-} ions for all other electrolytes to avoid their interaction with the pH sensor. In contact with the KCl solution in the pH sensor, KClO_4 was formed, clogging the frit between the electrolyte in the cell and in the pH sensor due to its low solubility in water.

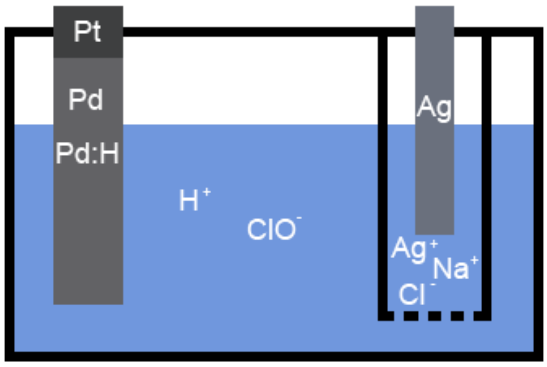

Figure 3.2: Schematic diagram of the setup used for Pd:H measurements

For eq. 3.5 and 3.6, a potential-determining redox couple at the Pt QRE cannot be identified. On the reference electrode side an equilibrium between silver ions and metallic silver is established, yielding the reference potential, E=0.209 V vs SHE [17]. The other junction that cannot be neglected without consideration is Pt|Pd. Since this junction was not fully sealed in glass, but placed in a glass capillary above the electrolyte, the presence of electrolyte between the dissimilar wires could not be excluded. In this case, local cell action between the platinum and the palladium would charge the palladium-hydride fully into the β - phase [18]. The potential in the β - phase is E = 0 mV vs RHE [16]. Since this potential was never observed, it is safe to assume that the charging reaction did not take place. Components in electrolyte not mentioned in chemical reactions were added to increase the conductivity of the electrolyte or to stabilize ions in solution.

3.2 Voltammetric behaviour

In order to determine suitable experimental conditions for hydrogen loading of Pd, cyclic voltammograms were measured in 0.1 M $HClO_4$. Figure 3.3 shows a cyclic voltammogram in the same configuration as later used for loading, that is, for a flame-annealed Pd wire immersed over ca. 5 mm in the electrolyte. The measurement starts at the open circuit potential (OCP) = 0.7 V vs. SHE, and proceeds first in negative direction. Immediately on passing the thermodynamic potential of hydrogen reduction (0 V vs SHE), a reduction current flows that increases until -1 V. Up until this point, almost no hydrogen evolution bubbles can be observed at the Pd wire. On crossing

the peak at -0.9 V, clearly more hydrogen bubbles are formed. At potentials below -2 V, ohmic losses in the cell dominate the response and yield a straight current-potential curve. On the return scan, almost the exact inverse trajectory is followed for negative potentials. For positive potentials, a very broad peak is observed with its maximum at +2 V. Repetition shows no pronounced differences from cycle to cycle.

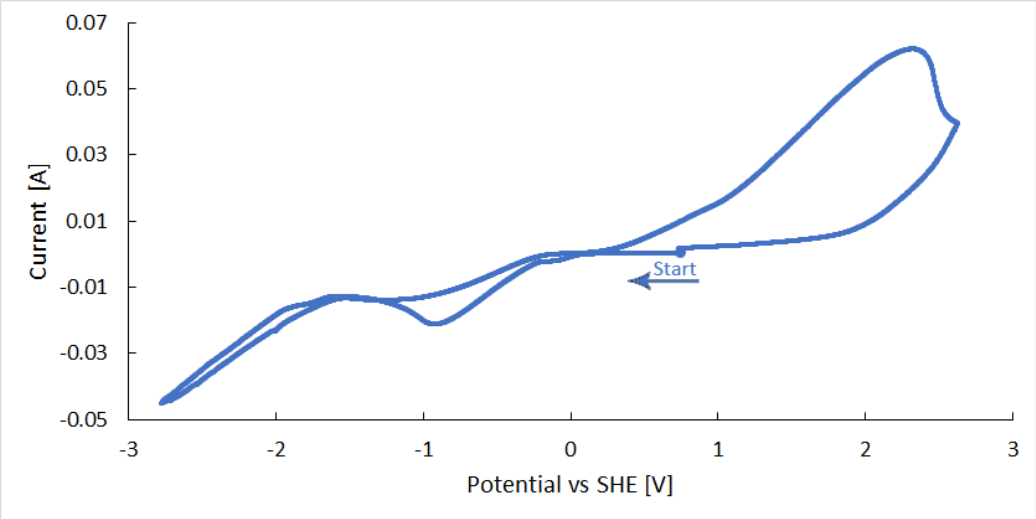

Figure 3.3: Cyclic voltammogram of Pd in 0.1 M $HClO_4$ vs Ag/AgCl

We interpret the peak at -0.9 V as directly related to the dissolution of atomic hydrogen in the Pd lattice. The observation of a peak may indicate that the rate of dissolution at this point becomes the limiting factor. For positive potentials, oxidation at the surface of hydrogen that diffuses out of the Pd:H lattice is measured, forming the peak at +2 V, but at some point it is accompanied by oxidation of Pd itself, oxidation of the solvent and oxygen evolution.

During preliminary experiments, it was found that no stable Pd:H electrodes could be produced unless reduction currents of at least 30 mA were reached. Inspection of the cyclic voltammogram in figure 3.3 shows that this necessarily corresponds to potentials negative from -2 V, that is, well negative from the hydrogen reduction peak. The clear reductive peak at -0.9 V may therefore also be a signature for completion of the α-phase.

3.3 Preparation

The palladium-hydrogen reference electrodes were prepared by galvanostatic electrolysis in 0.1 M $HClO_4$. The palladium wire was flame-annealed for about one minute, left to cool in air for at least five minutes, and then immersed into the $HClO_4$ solution. The open OCP was measured for four minutes, to compare the initial state of different measurements. This step could be omitted in future, since the OCP before loading showed no correlation to the potential after loading.

Cathodic current was applied in six 5-second windows, each followed by 30 s OCP measurement. Finally, anodic current was applied for 5 s. When hydrogen is reduced at the Pd wire surface and diffuses into the bulk, a hydrogen concentration gradient from the surface into the bulk is established. While this gradient is too steep, the stable potential aimed for is not observed. The anodic current removes hydrogen from the bulk with the inverse dependence on the distance from the surface, flattening the concentration gradient to yield the desired stable potential [13].

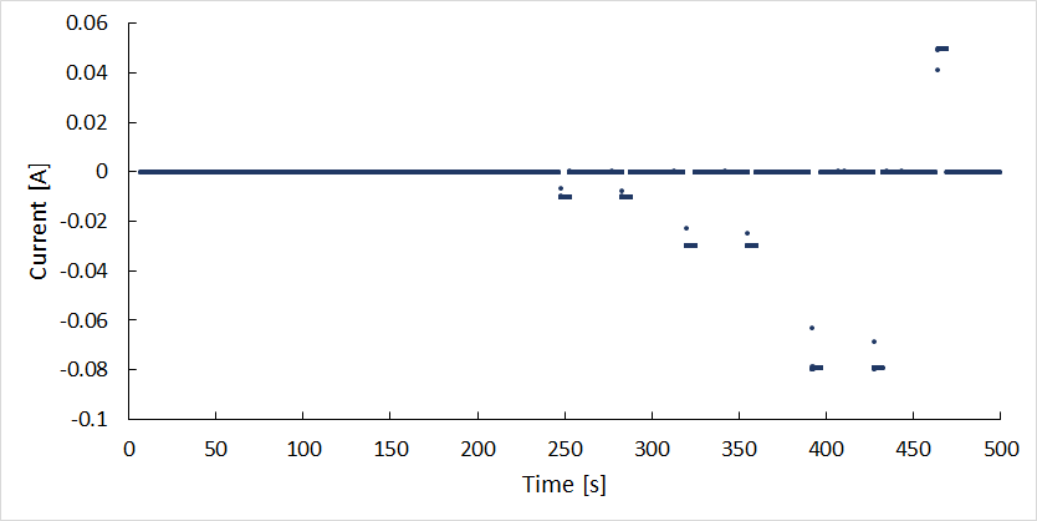

Figure 3.4: Galvanostatic current-time profile for loading Pd with H

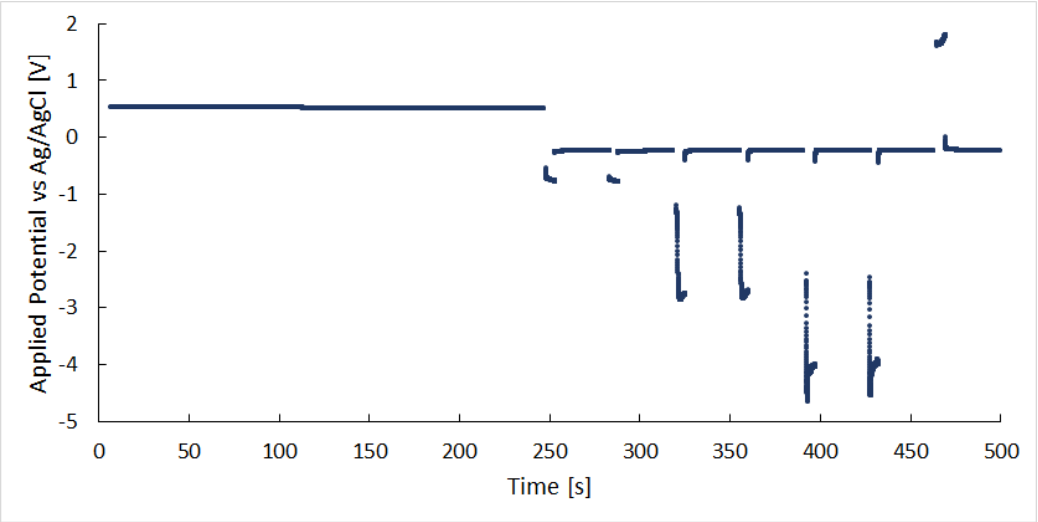

Figure 3.5: Potential-time profile during galvanostatic loading of Pd with H

The entire current-time profile during loading, including OCP measurement, is shown in figure 3.4, and the accompanying potential-time profile in figure 3.5. The potential required to produce the galvanostatic current showed a training effect, it decreased with the number of loading cycles.

The preparation is based on the method published by Vasile and Enke [13], who use much smaller current densities for 24 hours to load the palladium, and anodize for variable time until the potential reaches the desired value of +50 mV versus RHE. While this method claims to achieve better stability of the resulting reference potential, 1 mV/24 hours compared to 10 mV/10 hours in pH 1 under argon atmosphere, priority was given to fast loading of reference electrodes.

Pd wires were cooled in argon atmosphere and loaded in electrolyte for the first experiments, to avoid reactions with oxygen in the loading process. Identical cyclic voltammograms in the potential range used for loading were acquired in presence and absence of oxygen. Electrodes were since cooled in air and loaded in electrolyte in equilibrium with air.

Cells with a separated counter electrode compartment were necessary to consistently produce stable Pd:H electrodes. In a single-compartment cell, the first two electrodes produced with new electrolyte exhibited the stable potential plateau as usual, while electrodes produced after that would give up the potential after less than 10 hours (cf. section 3.5). In a cell with separated

counter electrode compartment, the same electrolyte could be used for 70 loading cycles without an appreciable effect on stability.

3.4 pH Response

H^+ is the oxidized species in the potential-determining reaction of the Pd:H electrode (eq. 3.1), so its activity in solution gives a_{Ox} in the Nernst equation (eq. 2.1). Therefore, the Pd:H electrode potential E depends on the logarithmic activity of H^+ in solution with

$$E = \frac{RT}{nF} * \ln\, a_{Ox} + \text{const.} \;\; = \frac{RT}{nF} * (-\text{pH}) + \text{const.} \tag{3.7}$$

While the right side of the potential-determining reaction 3.1 was discussed theoretically in section 3.1 and experimentally in section 3.2, measuring the pH response allows to confirm the left side of the potential determining reaction of the constructed electrode.

To measure the pH response of the Pd:H system, electrodes were prepared as discussed in section 3.3, and for all data points except pH=1.1 rinsed with ultrapure water and transferred to a second cell containing electrolyte of the desired pH. After closing the cell, argon purging was continued for another 20 minutes. The electrolyte for pH 1.1 was 0.1 M (= 0.1 mol/l) $HClO_4$, all other unbuffered solutions (pH 3, 5, 6, 8, 10) were 0.1 M Na_2SO_4 the pH of which was adjusted with 1 M H_2SO_4 or 1 M NaOH. During transfer, the Pd:H electrode was exposed to air for less than 60 s. Measurements in $HClO_4$ in which the Pd:H electrode was deliberately exposed to air for 30 s to 5 minutes showed a small positive effect on electrode stability. Since the Pd:H electrodes to be used as reference electrodes in the EC-STM are loaded in the same cell as the Pd:H electrodes for stability measurements, and then rinsed in water and exposed to air for about 30s during transfer to the STM cell, effects of rinsing and air exposure affecting electrode potential and stability in the EC-STM are included in the measurements presented in this section.

As discussed in section 3.1, the Pd:H electrode should show a pH response identical to a reversible hydrogen electrode, specifically $E = 0.05V - 0.059V * pH$ vs SHE. The measured potentials as a function of pH are shown in figure 3.6, with error bars indicating not the standard error, but all potentials measured during the first 10 hours of each experiment.

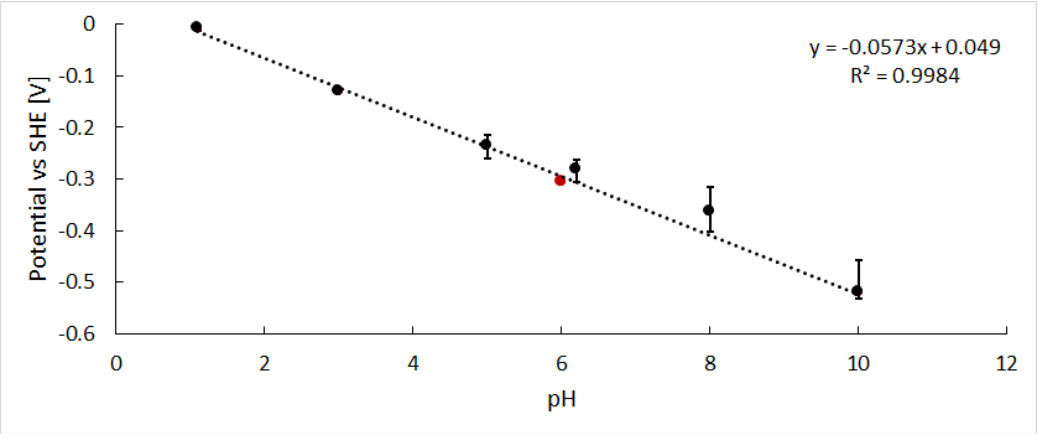

Figure 3.6: pH dependence of Pd:H electrode potentials. Black markers, unbuffered solutions; red marker, buffered solution. Error bars indicate full potential range measured over 10 hours. Fit through data points at pH 1.1, 3, 6, 10 as shown. See text for the reason of choosing these data points.

The potential shows the expected Nernstian behavior, with the fitted curve through the data points in unbuffered electrolyte being $E = 0.0488V - 0.0548V * pH$ vs. SHE. The squared Pearson product-moment correlation coefficient $R^2 = 0.9969$ indicates that the linear function is indeed a very good approximation for the data points. The deviation of the coefficients from the ideal curve $E = 0.05V - 0.059V * pH$ can be attributed to variations in the actual pH. While pH measurements in the most acidic solutions showed good stability over several days (pH 1.07-1.14 and pH 3.00-3.05), unbuffered solutions close to pH 7 were far less stable. The lack of pH stability is directly reflected in the range of potentials experimentally found. In order to test this hypothesis, potential measurements of the Pd:H electrode were performed in a phosphate buffer at pH 6, 0.012 M Na_2HPO_4 + 0.088 M NaH_2PO_4. In buffered solutions, a weak acid and its conjugated base determine the pH, and absorb small fluctuations of H^+ or OH^- concentration. Figure 3.7 compares the unbuffered and buffered measurements. The potential of Pd:H in buffered solution at pH 6 (red, dotted curve) is stable to the detection limit of the potentiostat, while the potential in unbuffered solution aimed at the same pH (red, solid curve) fluctuates with pH. The potential in unbuffered solution at pH 10 (blue, solid curve) is shown for comparison, on the same scale. Here the range of measured potentials is also larger than in highly acidic electrolyte, but stable for any single measurement. We attribute the larger range of measured potentials to low concentration of protons in alkaline solution.

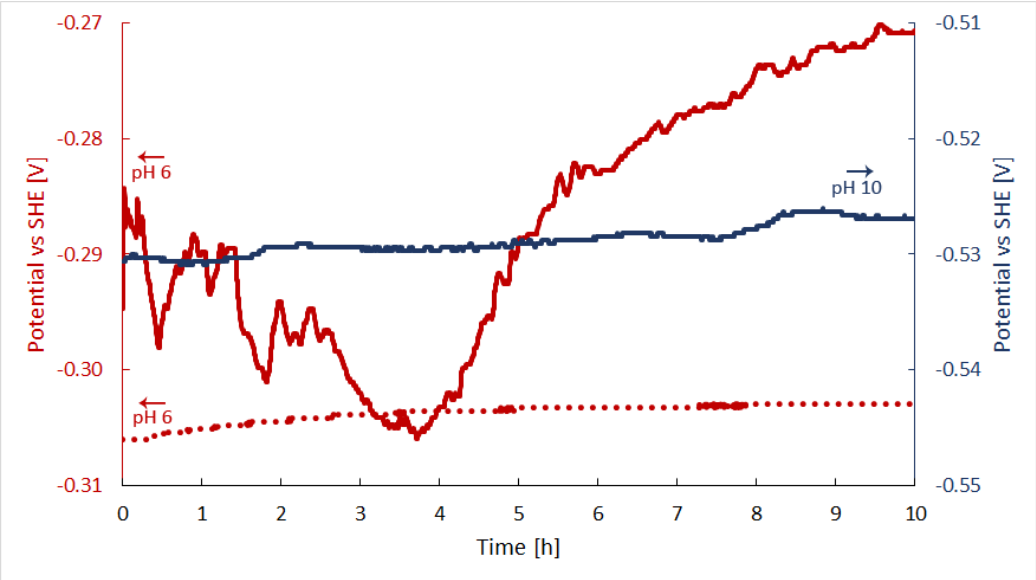

Figure 3.7: Potential of Pd:H electrode vs SHE over time, red curves at pH 6, blue curve at pH 10, solid curves in unbuffered and dotted curve in buffered solution

Figure 3.6 shows the potential of Pd:H over pH and the corresponding linear fit using only data points acquired in stable pH. This new fit $E = 0.049V - 0.0573V * pH$ vs. SHE is in very good agreement with the theoretically expected $E = 0.05V - 0.059V * pH$.

In summary, the Pd:H electrode showed both the potential and the pH response predicted by the Nernst equation.

3.5 Stability over Time

Over time, the potential of a palladium-hydrogen electrode exhibts an s-shaped curve, as shown in figure 3.8. The large step-like increase in potential is attributed to depletion of hydrogen in the palladium. After the step-like transition, the Pd wire behaves like a quasi-reference electrode, since one of the redox partners required for Nernstian behaviour is no longer present.

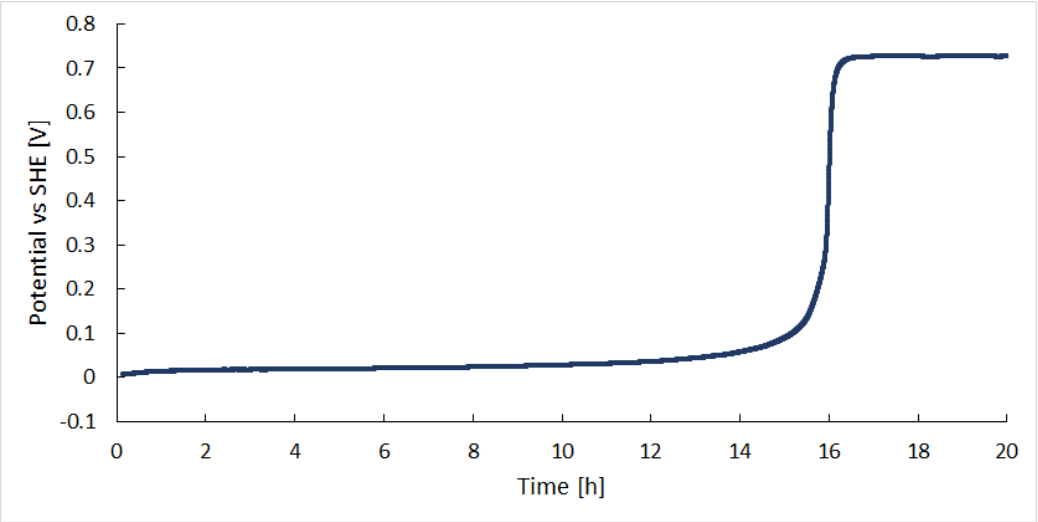

Figure 3.8: Measured potential of Pd:H over time, 0.1 M $HClO_4$, pH 1.1, in air

The time at which the hydrogen is depleted varied with loading conditions and with the measuring environment. With the preparation detailed in section 3.3 and the electrolyte in contact with air, depletion was observed after 15 to 20 hours. In argon-purged electrolyte, depletion was only observed after at least 20 hours. In case the electrode was prepared in a cell without separate counter electrode compartment, depletion is regularly observed after less than 10 hours.

All these observations indicate that the presence of oxygen leads to faster depletion of hydrogen. The decreased stability of palladium-hydrogen electrodes loaded in a cell without separate counter electrode compartment can also be attributed to the oxygen generated during loading cycles. It can be reduced to water at the cathode during the next loading cycle, carrying part of the current that would otherwise have been used for reducing water to hydrogen. This decreases the overall amount of hydrogen formed and loaded. Why the smaller but still non-negligible oxygen concentration found in electrolyte in equilibrium with air does not cause the same problem is still unclear.

3.6 Comparison with Pt quasi-reference electrode

Before the experiments with the Pd:H reference electrode started, a Pt QRE was used in the EC-STM. This comes with several downsides, mainly the uncertainty of the reference potential, coupled with absence of a well defined potential determining reaction, the fluctuations of the reference potential, and the increasing uncertainty of the reference potential with increasing pH value. Potential and stability of the platinum electrode were measured under the same conditions as for the palladium-hydrogen electrode, both to obtain a conversion for previous measurements and experience values, and to quantify the obtained improvement.

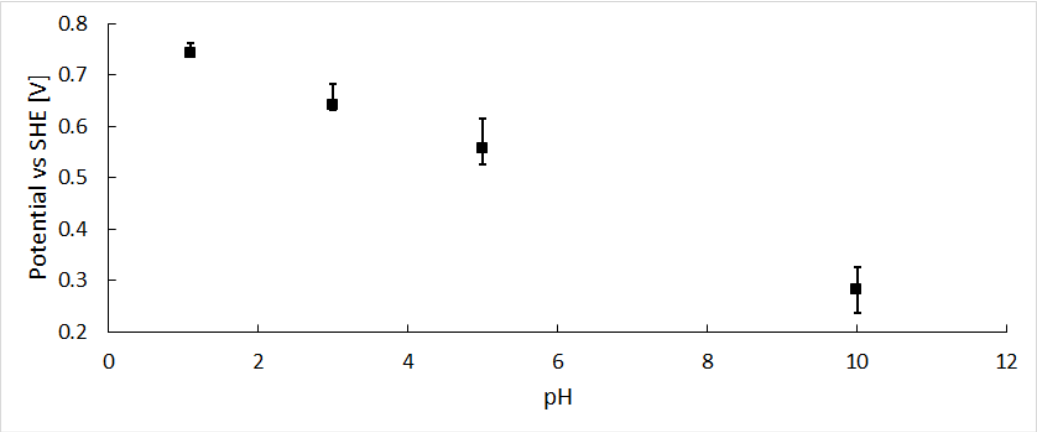

Figure 3.9: Potential of Pt electrode vs SHE over pH

A platinum wire (diameter 0.5 mm) was flame-annealed and cooled like the palladium wire (cf. section 3.3). The obtained potentials are shown in figure 3.9.

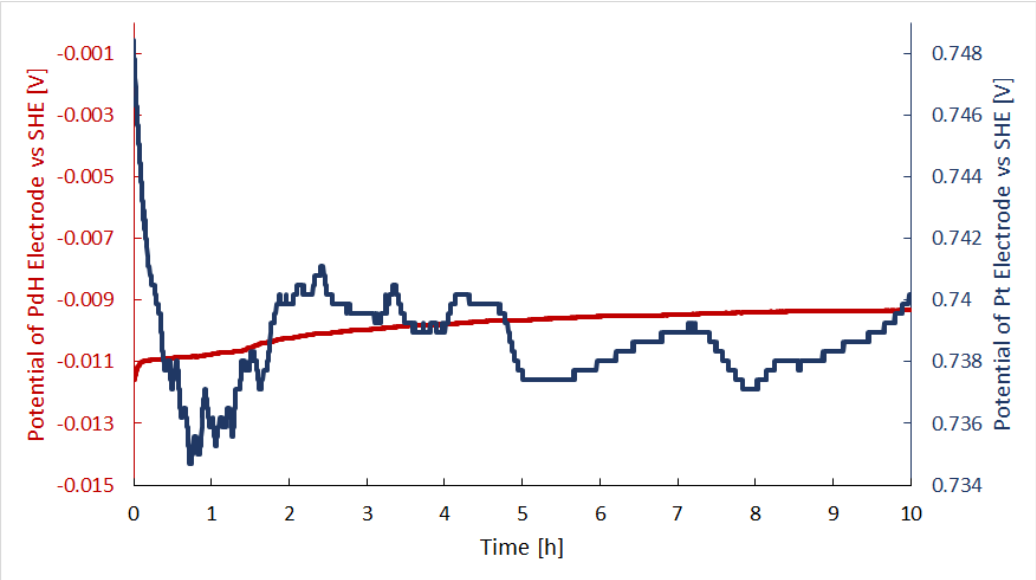

Figure 3.10: Potential of Pd:H (red) and Pt (blue) electrodes in 0.1 M $HClO_4$ pH 1.1, in Ar atmosphere

Figure 3.10 shows a direct comparison between Pt QRE and Pd:H. The potential of the platinum electrode exhibits a steep drop during the first hour, duration and magnitude of which increase with the pH of the electrolyte, followed by a comparatively stable value during the rest of the measurement. However, even when the plateau is reached, the potential still fluctuates appreciably, while the potential of the Pd:H electrode shows no short time fluctuations.

3.7 Effects on STM Measurements

The introduction of the palladium-hydrogen reference electrode into the EC STM provides three main advantages:

Data obtained can be related to a reliable reference potential, effectively increasing its scientific value. Also, experience with the probed systems can be acquired and transferred more easily. Knowing the potential values at which the system exhibits the desired behaviour allows for quicker measurements and avoidance of mistakes. By relating the values measured in the EC STM to a known reference potential we can use potentials from publications by simply transforming them to potentials vs Pd:H, we can relate measurements taken with the potentiostat to measurements in the EC STM, and we

can rely on our own experience values from previous measurements. Lastly, switching to the palladium-hydrogen electrode has made the approach of the STM tip much more stable, which not only saves time but also increases the chances of arriving at tunneling distance with a suitable STM tip. The potentials applied to sample and tip are relative to the reference potential, so if the latter fluctuates, they all do. Fluctuations in the tip potential induce changes in the tip current, requiring the approach with a higher stop current, which increases the chance of crashing the tip. Moreover, fluctuations in the tip potential can create reactions at the tip, which may make it unsuitable for STM even before any tip-sample interaction occurs, for example by covering it with a non-conductive product.

In summary, data against a stable and reliable reference potential is both more easily obtained and more valuable.

4 Oxygen Removal

4.1 Theoretical Background

In open *in situ* STM systems oxygen may interfere with the experiment by inducing additional redox processes. These can alter the sample, interfere with tunneling or influence electrode potentials, all of which must be avoided [19]. Oxygen can be removed from the electrolyte through equilibration with an oxygen-free atmosphere, specifically by a stream of dry Ar.

Assuming only diffusion takes place, this process is described by Fick's second law

$$\frac{\partial c}{\partial t} = D\frac{\partial^2 c}{\partial x^2} \tag{4.1}$$

with the boundary conditions

$$c_{(x>0,t=0)} = c_0 \tag{4.2}$$

$$c_{(x=0,t)} = 0 \tag{4.3}$$

We are looking at a diffusion process where only one coordinate is of interest, along the x axis from the solid-liquid interface to the liquid-gas interface. This is the only axis with a driving force for diffusion, yielding no net diffusion along the y and z axis. For calculations the concentration c of oxygen in the gas phase is assumed to be zero, as oxygen transported there is displaced quickly by the comparably large stream of gas. Since there is no barrier preventing oxygen from diffusing from the liquid to the gas phase, the concentration at the the liquid-gas interface must equal zero as well. D is the diffusion constant of the observed species in the medium.
A suitable *ansatz* to solve this problem is

$$\frac{c}{c_0}(x,t) = \mathrm{erf}\left(\frac{x}{2\sqrt{Dt}}\right) \tag{4.4}$$

with the error function erf(x) defined as

$$\mathrm{erf}(x) = \frac{2}{\sqrt{\pi}}\int_0^x \mathrm{e}^{-t^2}dt \tag{4.5}$$

and shown in figure 4.1.

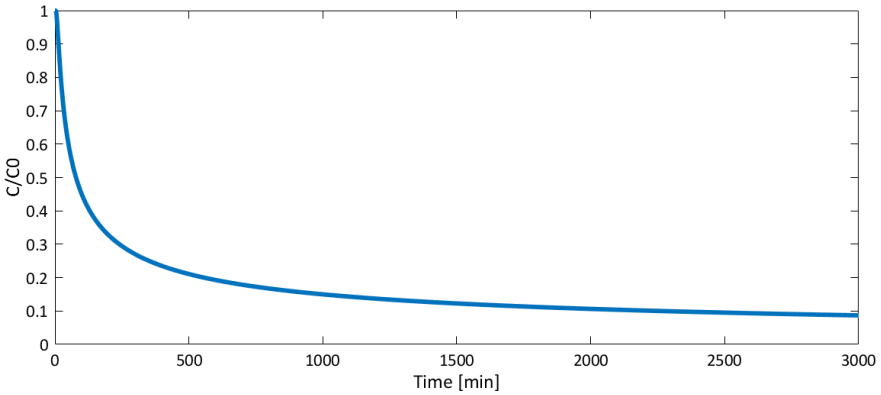

Figure 4.1: Diffusive decrease of concentration over time

Since the information of interest is the time t to remove oxygen from a cell with the depth x_0, the result is transformed to

$$t = \frac{x_0^2}{4 * D * \text{inv erf}^2\left(\frac{c}{c_0}\right)} \tag{4.6}$$

The electrolyte will be oxygen-free at $\text{erf}\,(c = 0) = 0$ and thus $t = \infty$. 10 % of the original concentration can be reached after 30 hours, 30% after 3 hours, and 50 % after 1.3 hours, assuming a cell depth of 3 mm, a diffusion constant for oxygen in water of $D = 2.1{*}10^{-9}$ m^2s^{-1} [20] and purely diffusive transport.

The flow of dry argon through the chamber causes water in it to evaporate, yielding changes of the concentration of the electrolyte. To avoid this, a reservoir of water with a much larger surface area (100 cm^2 versus 0.4 cm^2) than the electrolyte in the STM cell was used in the environmental chamber, figure 4.2. As evaporation consumes energy and could aggravate thermal drift in the system, we estimate an upper limit for the cooling of the STM cell.

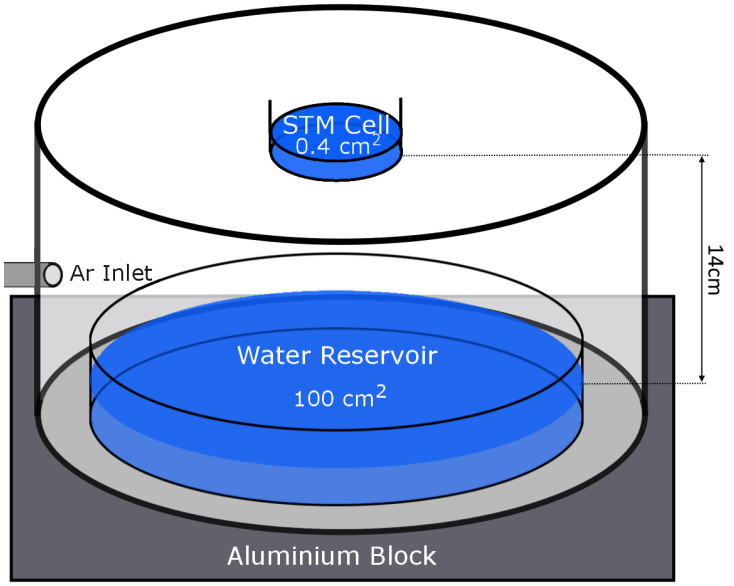

Figure 4.2: Schematic diagram of the environmental chamber

We first estimate an upper limit for water evaporation inside the chamber. Assuming 1 liter of replaced atmosphere per minute, fast enough evaporation to keep the atmosphere saturated with water, and a temperature of 300 K, the ideal gas law yields:

$$m = \frac{M * p * V}{R * T} = 2.3 * 10^{-5} \frac{kg}{min} \tag{4.7}$$

with M = 0.018 $\frac{kg}{mol}$ the molar mass of water, p = 3170 Pa the saturation vapor pressure of water in air at 300 K [21], V = 10^{-3} $\frac{m^3}{min}$ the replaced volume per minute, R = 8.3 $\frac{J}{mol*K}$ the universal gas constant and T = 300 K the temperature. With the evaporation energy of water 2.5 $\frac{MJ}{kg}$ [21], this consumes 57 $\frac{J}{min}$, cooling the water in the STM cell (0.023 kg with the assumed cell depth of 3 mm) by 0.6 $\frac{K}{min}$.

Thermal conductivity can be described with the same equations used to describe diffusion. Thus, thermal conductivities λ add reciprocally like diffusivities and electrical conductivities. To reach the water reservoir from the sample, heat must cross a barrier of 14 cm of argon. To reach the water reservoir from the aluminium block below, which we treat as an infinite heat sink due to its good thermal conductivity and contact with the ambient air, heat needs to cross about 2 mm of water, 2 mm of glass and about 0.1 mm of Ar

separating the glass petri dish from the metal support due to surface roughness. With thermal conductivities of $\lambda_{Ar} = 0.0179$ J/smK, $\lambda_{H2O} = 0.5562$ J/smK and $\lambda_{Glass} = 0.76$ J/smK [21] and $\frac{d_{H2O}}{\lambda_{H2O}} + \frac{d_{Glass}}{\lambda_{Glass}} + \frac{d_{Ar}}{\lambda_{Ar}} = \frac{d_{H2O->Al}}{\lambda_{H2O->Al}}$ the fraction of the evaporation cooling that goes to the sample and not to the aluminium block is:

$$\frac{\lambda_{H2O->STM} * d_{H2O->Al}}{d_{H2O->STM} * \lambda_{H2O->Al}} \approx 10^{-3} \tag{4.8}$$

Assuming that all gas removed from the ambient chamber is saturated with water and that the STM cell is an infinite heat sink, the sample is cooled by 0.057 $\frac{J}{min}$, cooling a body of 1.2*10^{-4} kg of water by 0.1 $\frac{K}{min}$, all in case of pure thermal conduction. This upper limit indicates that evaporative cooling may indeed pose a problem in our system.

4.2 Experimental Procedure and Results

Oxygen is removed from the electrolyte by replacing the air around it with argon, removing the oxygen in solution by diffusion as detailed in section 4.1. The glass chamber (volume of 5.8 l) around the EC-STM cell was flushed with 2.25 l/min of argon for 15 minutes to quickly remove air from the environmental chamber, and from then on with 1 l/min of argon to remove the oxygen diffusing out of the electrolyte and to limit back-diffusion into the chamber. The observed evaporation rate from the petri dish while dried argon flows through the chamber as described above is 3*10^{-5} $\frac{kg}{min}$, which is close to 2.3 * 10^{-5} $\frac{kg}{min}$, the estimate from equation 4.7.

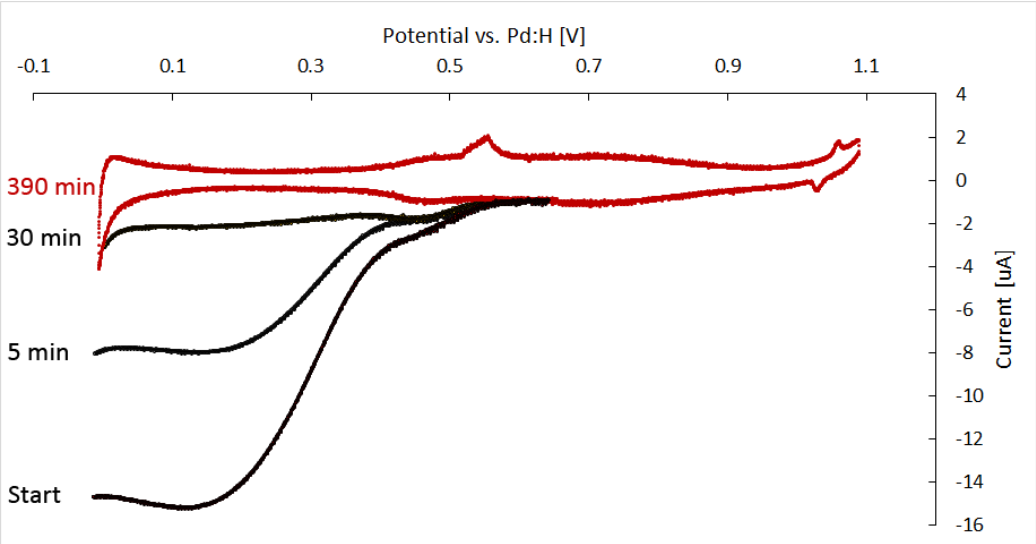

Figure 4.3: Electrochemical determination of oxygen removal from the EC-STM cell, on Au(111) in 0.1 M H_2SO_4, purging time as indicated, scan rate 50 mV/s

Oxygen in solution was measured electrochemically, by reduction at the (111) surface of an Au crystal mounted in the EC-STM cell (figure 2.3), which was filled with 130 μl of 0.1 M H_2SO_4. After a very long time of purging with Ar, the typical CV for Au(111) in sulfuric acid solution is obtained, figure 4.3, red trace. The broad capacitive peak at about 0.5 V originates in the onset of sulfate ion adsorption. As the potential is made more positive, the interfacial capacitance decreases until a phase transition is reached at +1.05 V, characterised by a pair of sharp peaks. At the negative limit of the voltammogram, the onset of hydrogen evolution is visible.

When oxygen is present in solution, reduction features are superimposed on the Au(111) voltammogram at potentials < 0.5 V. In acidic solution on gold, the main process is the 2-electron reduction yielding hydrogen peroxide [22]:

$$O_2 + 2e^- + 2H^+ \rightarrow H_2O_2 \tag{4.9}$$

As the potential is made more negative, the initially increasing current reaches a plateau at which point transport in solution becomes rate-limiting. It can be shown that the current value of the plateau is proportional to the concentration of the electroactive species, here oxygen [17].

The oxygen reduction current was evaluated at 0.15 V, and corrected for non-faradaic current assuming no remaining faradaic current after 6.5 hours of

oxygen removal. The electrode area of 10.6 mm^2 to calculate current densities was measured by oxidation of 0.1 M $K_4\,[Fe\,(CN)_6]$ on the Au(111) electrode, with the sealing ring used for all STM measurements shown in this thesis, compared to a rod-shaped gold electrode with a known electrode surface area of 1.6 mm^2. The potential of the Pd:H reference electrode changes in presence of oxygen (cf. section 3). Potentials are offset by the measured change in the open circuit potential of Au(111) to correct for this shift.

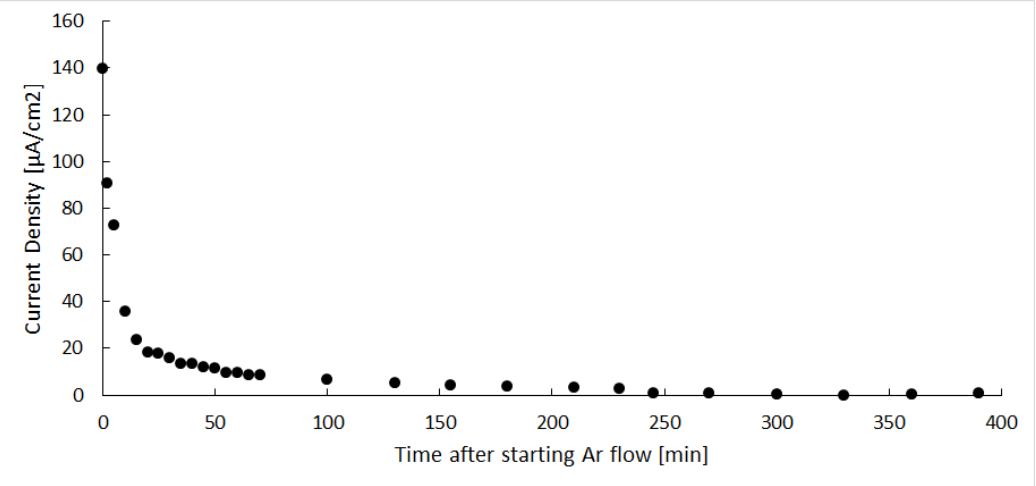

Figure 4.4: Oxygen reduction current on Au(111) while displacing oxygen

Figure 4.4 shows the oxygen reduction current over time. It decreases with time as expected, but considerably faster than diffusion alone can explain. The measured oxygen concentration drops below 10% of the initial concentration in 35 minutes, compared to 30 hours calculated in section 4.1. We ascribe this difference to convective processes originating in, e.g., mechanical vibrations and temperature differences in the system.

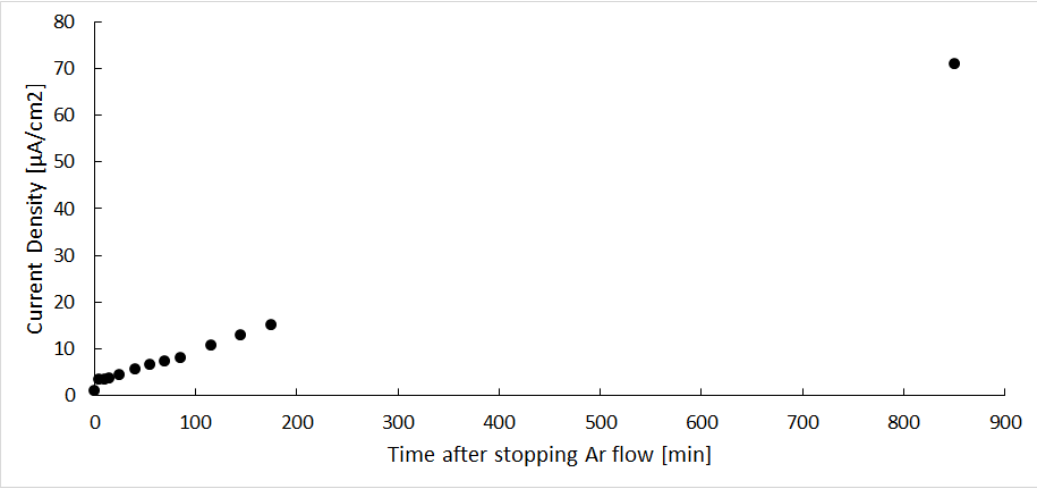

Figure 4.5: Oxygen reduction current on Au (111) after switching off argon flow

The time it takes for oxygen levels to rise after switching off the argon flow is shown in figure 4.5. The observed behavior is not proportional to an error function, as it would be for diffusion, but linear. This linear time dependence suggests that the limiting factor is not the movement of oxygen through the solution, but the concentration of oxygen available in the gas phase, which increases linearly with time as air flows into the ambient chamber. The observed behavior can be compared to the zero-order reaction kinetics observed in a system where one reactant becomes available at a small and constant rate. When the reaction or diffusion proceeds faster than the reactant becomes available, the kinetics are determined by the availability of the deficient reactant, which can be supplied with a linear time dependence via dissolution or passing through a small opening [23].

4.3 Effects on STM Measurements

Oxygen can limit the resolution in STM, and even influence the state of the probed system, by reacting with it. It has also been suggested as a scattering center for the tunnelling electrons [19], conclusive evidence for which is still lacking.

We have obtained clearer STM images after removing oxygen, as shown in section 5, and we now have the possibility to study systems sensitive to oxygen. The absence of oxygen stabilizes the reference potential and increases

its stability time (cf.section 3). The absence of oxygen also stabilizes the platinum iridium tips' response to the potential applied, increasing the available range of bias voltage available for scanning at a given sample potential. Thirdly, by keeping the sample in a controlled atmosphere, we are able to keep it for three consecutive days of measurements in the STM cell without cleaning. Piezo drift after the first approach, as well as other non-equilibrium effects in the cell stand in the way of obtaining good images, especially during the first hours after assembly. To give the system enough time to equilibrate, and to increase the ratio of available time for measurements over time for sample preparation, it was of interest to be able to keep the sample in the EC STM for longer than one day between cleaning cycles.

In summary, in an oxygen free system, we can obtain better images, over a wider range of tunneling conditions, and we have more time to do so.

5 Electrochemical STM on Rutile TiO_2 (110)

5.1 Introduction of Platinum Iridium Tips

Initially, EC-STM imaging was carried out using tungsten tips. These tips are the easiest to etch to the sharpness required to achieve atomic resolution. However, it was found that tungsten tips dissolve in the EC-STM. Metallic tungsten is thermodynamically unstable under all experimental conditions accessible in the EC-STM, leading to formation of tungsten oxide, which readily adsorbs on the TiO_2(110) surface [24], as shown in figure 5.1.

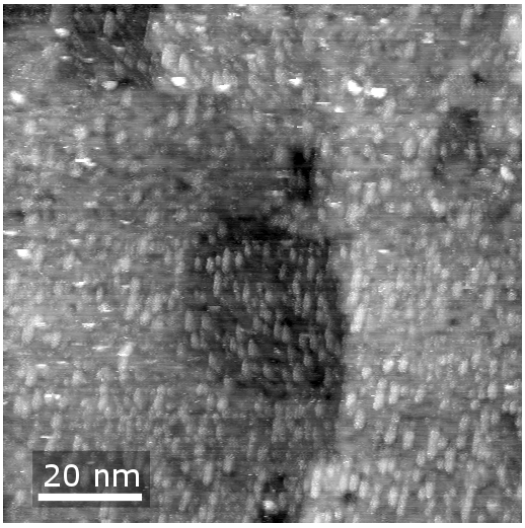

Figure 5.1: EC STM image of rutile TiO_2(110) with tungsten oxide adsorbates, E_{sample}=0.3 V, E_{tip}=-1.12 V vs Pt, I=0.3 nA, in 0.1 M $HClO_4$ [160510_170642]

For this reason, W tips were replaced with Pt-Ir tips. Following this change, *in situ* imaging of oxide surfaces was possible, for up to 72 hours, without sample cleaning or observation of tip-induced contamination.

PtIr tips are etched from a PtIr wire (80% Pt 20% Ir), in a 4 mol/l KSCN + 2 mol/l KOH solution, using a tantalum ring counter electrode. The etching voltage is a square wave with 1 kHz and 10 V_{pp}, and a DC offset of -2 V. The part of the wire that will form the tip is covered with a PTFE tube (Sigma-Aldrich, inner diameter 0.3 mm), to expose only a thin section of the wire to the electrolyte [25].

For EC-STM use, tips must be insulated to suppress faradaic current in the electrochemical environment. To this end, the tips were passed through a lamella of molten Apiezon wax heated to 150 °C, which coats the metal wire, while leaving the very end exposed. Apiezon wax was chosen from the tested coatings since it provided the smallest uncovered tip surface, which reduces leakage currents and thereby improves image quality as well as the chance to be able to approach a tip. The temperature to which the wax is heated before coating was optimized to yield the largest ratio of tips left with a conductive end over all coated tips. About 20 % of etched and coated tips were found to produce EC-STM images showing at least step-morphology. Rigorous testing was not possible, since many factors apart from tip quality influence whether images can be obtained in the EC-STM.

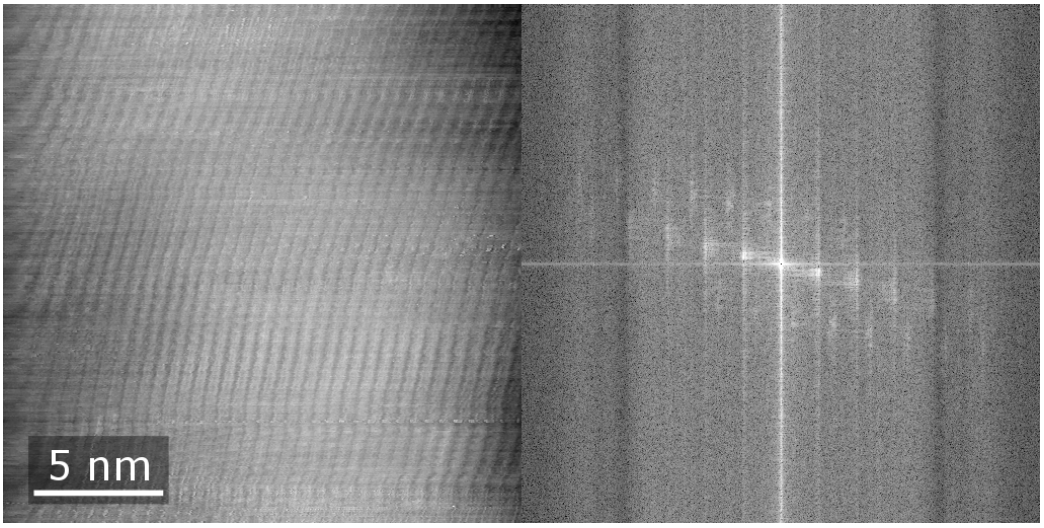

Figure 5.2: EC-STM image of rutile TiO_2(110) doped with 0.25 wt% Nb, E_{sample}=-0.4 V, E_{tip}=-0.7 V vs Pt, I=0.14 nA, in 0.1 M $HClO_4$ [160428_112624] and FFT of the same image

Figure 5.2 shows an image of the first set obtained with PtIr tips on oxides, on rutile TiO_2(110), doped with 0.25 wt% niobium to make the crystal conductive without reduction in UHV, using a Pt QRE, in 0.1 M $HClO_4$ in equilibrium with air. Atomic resolution was achieved, as confirmed by the fast Fourier transform (FFT) of the image. The lattice periodicity measured from the FFT is 5.2 Å, indicating a (1 × 1) reconstruction. We attribute the difference between the measured 5.2 Å and 6.5 Å (expected from the TiO_2(110) lattice periodicity along $[1\bar{1}0]$) to drift, and to the STM being calibrated for a different tip length than used for this specific measurement.

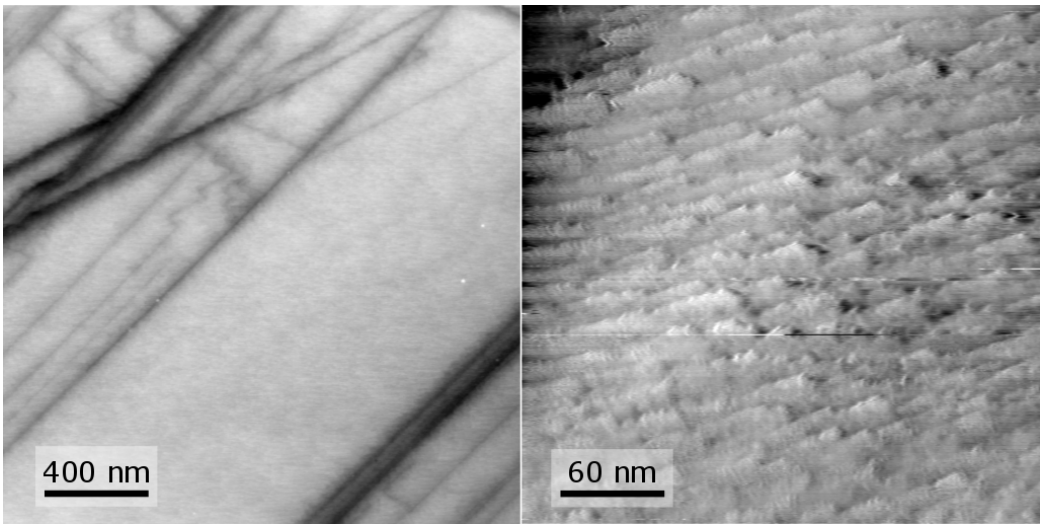

Figure 5.3: AFM image of rutile TiO_2(110) doped with 0.25 wt% Nb [160425_173438] and EC STM image of the same, E_{sample}=0.4 V, E_{tip}=-0.7 V vs Pt, I=0.12 nA, in 0.1 M $HClO_4$ [160429_113934]

The roughness of the sample, shown in figure 5.3, prompted a switch from niobium doped to pure TiO_2, made conductive as detailed in section 2.6. One of the best images of the set is shown in figure 5.4. Atomic resolution was not obtained, while step-morphology can clearly be discerned. The rectangular holes are attributed to the etching during the wet-chemical sample preparation [11].

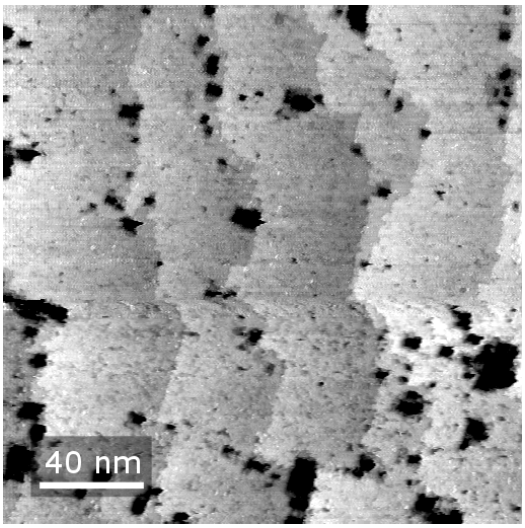

Figure 5.4: EC STM image of rutile TiO_2(110) measured with a PtIr tip, E_{sample}=0.516 V, E_{tip}=-0.97 V vs Pt, I=1.76 nA, in 0.1 M $HClO_4$ [160504_144656]

5.2 Improvements from Pd:H reference electrode and oxygen removal

The methodological refinements discussed in previous sections, in particular the use of a stable Pd:H reference electrode and oxygen removal, resulted in clearly improved EC-STM images. A representative example is shown in figure 5.6, comparison to image 5.4 shows the pronounced increase of image resolution.

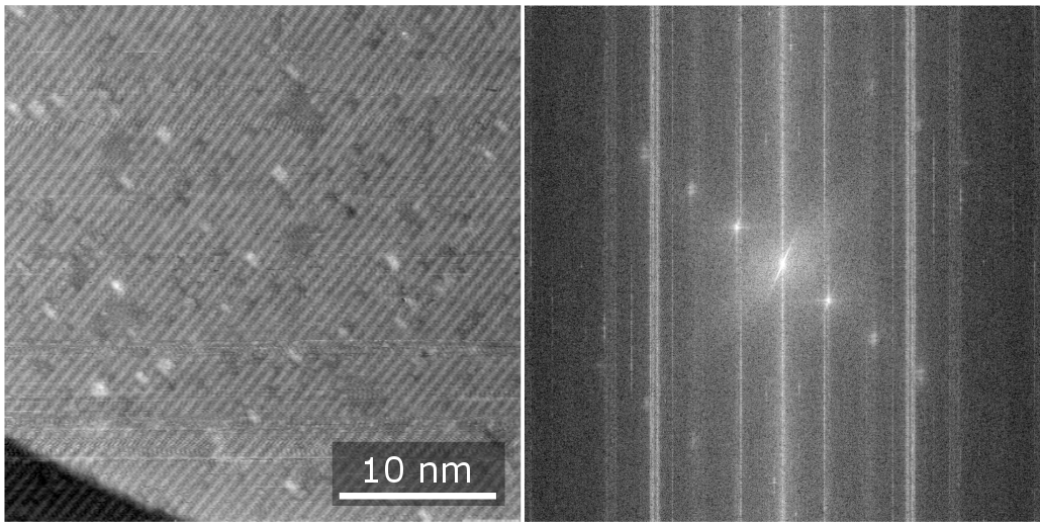

Figure 5.5: UHV STM image of rutile TiO_2(110), U_{bias}=1.2 V, I=0.13 nA [2253] and FFT of the same image

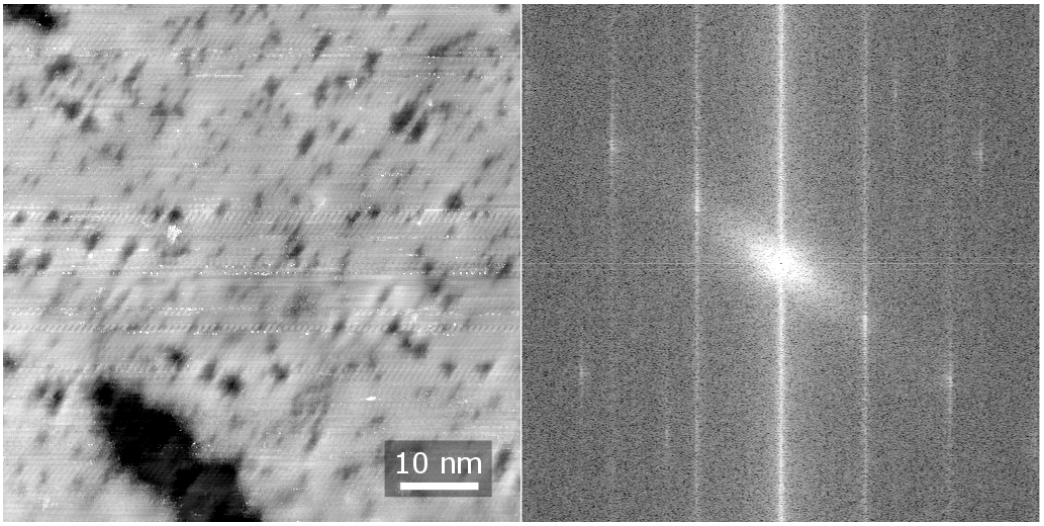

Figure 5.6: EC-STM image of rutile TiO_2(110) vs Pd:H under argon atmosphere, E_{sample}=0.382 V, E_{tip}=-0.205 V vs Pd:H, I=0.6 nA, in 0.1 M $HClO_4$ [160715_165915] and FFT of the same image

Figures 5.5 and 5.6 show images taken in UHV and in the EC STM, respectively. Both images show atomic resolution, as confirmed by the FFT. We see the bulk-truncated (1 x 1) structure commonly observed in UHV, alternating bright and dark rows along the [001] direction, where the bright rows are

associated with the rows of fivefold-coordinated Ti atoms [3]. In electrolyte, the same row-structure is imaged, while the electronic states tunnelled into may be those of water adsorbed on the Ti rows.

The sample was not cleaned between acquisition of the two images, it was taken out of UHV and transferred directly into the EC STM cell. The small dark features observed in image 5.6 can thus be related to similar features in image 5.5. They may have been caused by electrochemical sample preparation before introduction into UHV, or by sputtering with argon.

5.3 Adsorption of Benzoic Acid

Technological applications of TiO_2, such as higher efficiency dye-sensitised solar cells, require a molecular-level understanding of the materials and interfaces involved. A useful model system to study adsorption on rutile TiO_2(110), with technologically relevant structural analogues [26] [27], is benzoic acid ($C_7H_6O_2$), figure 5.7. This molecule has been studied in UHV, indicating dissociative adsorption with both oxygen atoms bound to the fivefold coordinated Ti atoms [28] [29] and the rings forming an edge-to-face structure [30].

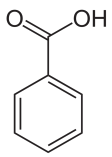

Figure 5.7: Structure of benzoic acid

In an attempt to directly observe benzoic acid adsorption *in situ*, rutile TiO_2(110) was imaged in a solution of 0.1 M $HClO_4$ + 0.01 M benzoic acid. However, no features that could be ascribed to adsorbed benzoic acid were detected in EC-STM. This may indicate that benzoic acid cannot compete successfully with hydroxyls for adsorption on the surface, but also too high a mobility of low-coverage adsorbates to allow imaging on the time scale accessible to STM. Higher concentrations of benzoic acid in solution, to shift the adsorption equilibrium, were not accessible in view of the limited solubility of the target molecule.

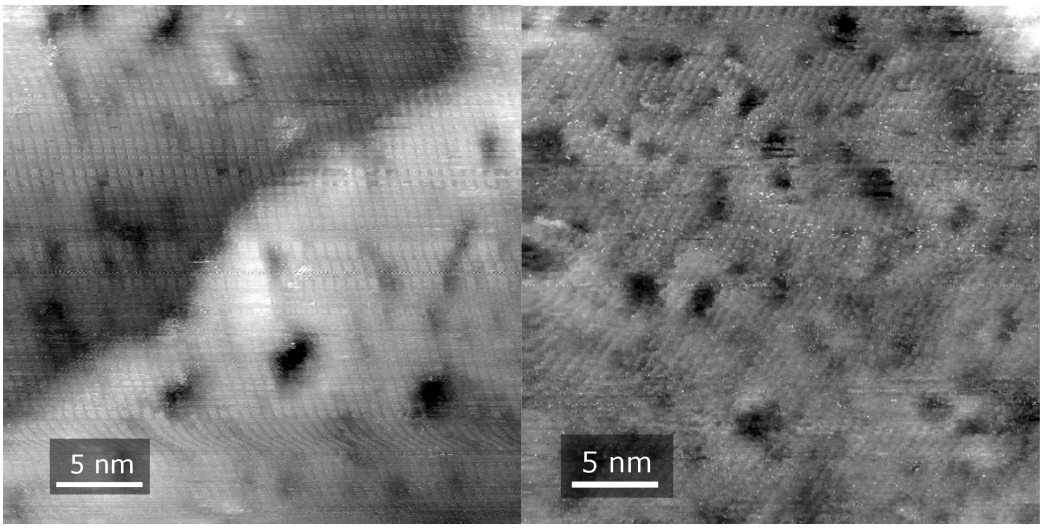

Figure 5.8: EC STM images of rutile TiO_2(110) in 0.01 M benzoic acid + 0.1 M $HClO_4$ (left, E_{sample}=1.17 V, E_{tip}=-0.2 V vs Pd:H, I=0.56 nA [160802_121539]) compared to the same surface in 0.1 M $HClO_4$ (right, E_{sample}=0.5 V, E_{tip}=-0.12 V vs Pd:H, I=0.27 nA [160720_174231])

5.4 Grafting of Aryl Radicals

More reactive adsorbates, where the formation of a covalent bond between adsorbate and substrate is virtually guaranteed, can resolve problems of adsorbate mobility. An example is the use of aryl radicals, which are prone to covalent grafting to almost any surface. Because of the very high reactivity of the *in situ* generated radicals, poorly controlled reactions leading to on-surface polymers are a probable result. Suitable precursors (here, a phenyl ring with bulky substituents blocking suitable sites for polymerization, figure 5.9) prevent such side reactions and lead to strict monolayer growth on the substrate. [31].

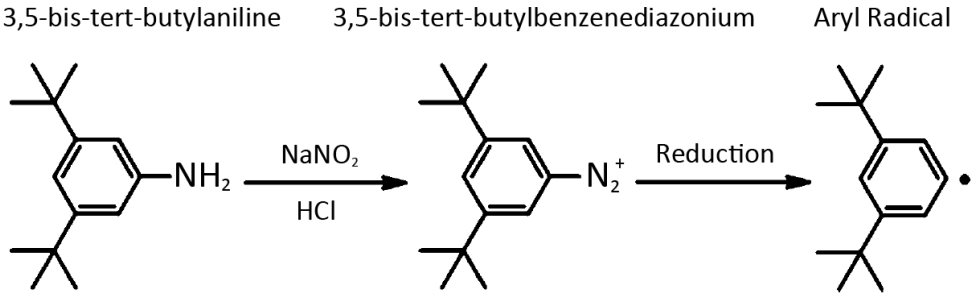

Figure 5.9: Reaction Scheme of 3,5-bis-tert-butylaniline via 3,5-bis-tert-butylbenzenediazonium to the aryl radical

To avoid its decomposition before the reduction, the 3,5-bis-tert-benzenediazonium (3,5-TBD) was synthesized from an aniline precursor immediately before use, via the reactions

$$NaNO_2 + HCl \rightarrow HNO_2 + NaCl \tag{5.1}$$

$$HNO_2 + ArNH_2 + H^+ \rightarrow ArN_2^+ + 2H_2O \tag{5.2}$$

where Ar denominates the aryl group. Upon reduction of 3,5-TBD on the TiO_2 surface, a neutral N_2 molecule is formed, leaving behind an aryl radical. The reaction scheme is detailed in figure 5.9. The mechanism suggested to bind the aryl radicals to the TiO_2 surface involves one radical taking up an H atom from a surface OH-group, leaving behind a dangling bond which is saturated with a second aryl radical [32].

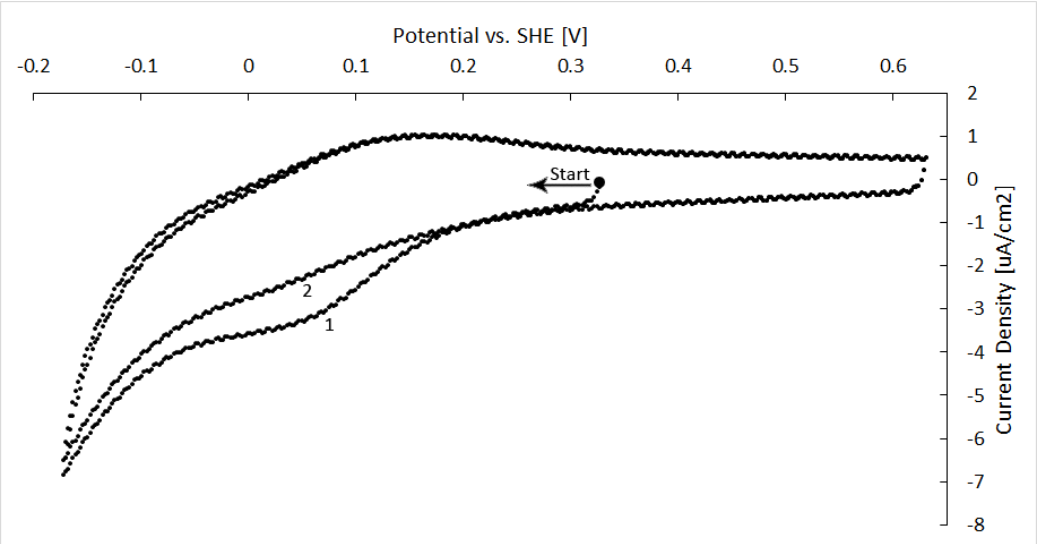

Figure 5.10: Cyclic voltammogram of TiO_2(110) while grafting 3,5-TBD

Figure 5.10 shows the cyclic voltammogram of the surface modification in 1 mM 3,5-TBD and 50 mM HCl. The reduction of the diazonium group can be observed between 0.15 V and -0.1 V vs SHE. The reduction current vanishes from the first to the second scan, indicating a modification of the surface that prevents further reduction of diazonium to radicals. In the scan performed in 0.1 mM 3,5-TBD the observed reduction current in the first scan is much smaller than in the experiment shown here, but still vanished from the first to the second scan.

After grafting, the sample was transferred from the voltammetric cell into the STM cell by disassembling the voltammetry cell, rinsing the sample and subsequently the sealing ring in ultrapure water to remove any physisorbed material, and then assembling the STM cell. Despite several attempts, no useful STM images were obtained with this procedure, possibly due to contamination. Between removal from the voltammetric cell and insertion of the electrolyte into the STM cell, the sample is protected from exposure to air only by a thin liquid film. During rinsing, water may flow not only from the clean surface towards the parts of the sample that have been contaminated during grafting, but also in the other direction.

During measurements, approaching a tip in a promising state was rarely possible, and on successful attempts it would change for worse on the first lines of the first scan. This behaviour fits with the assumption of a contam-

inated sample. Another explanation could be the tip collecting the radicals from the surface, which seems less plausible given the strength of the bond expected to be found between the radicals and the surface.

In order to measure on a clean sample, the surface was cleaned in alkaline piranha as detailed in section 2.6 after the experiment with aryl radicals grafted from 1 mM 3,5-TBD solution. Since the radicals were expected to bind to the TiO_2 surface strongly, and act as a protective layer on it, finding them on the surface after cleaning was plausible. An EC-STM image obtained with this preparation is shown in figure 5.11. The surface is much rougher than expected, exhibiting terraces only up to 10 nm in diameter. No grafted species could be identified in these images.

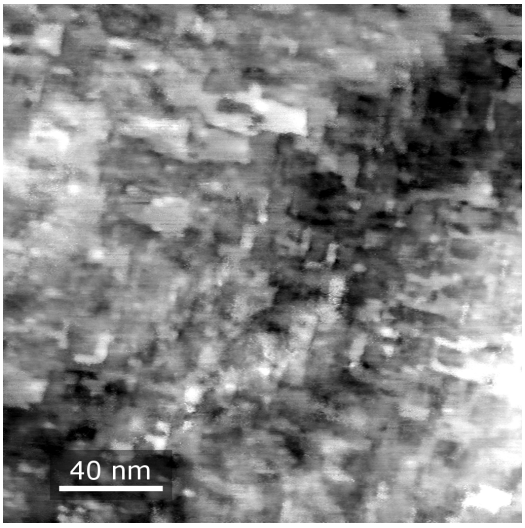

Figure 5.11: EC STM image of rutile TiO_2(110) after grafting experiments, E_{sample}=0.55 V, E_{tip}=-0.05 V vs Pd:H, I=0.2 nA, in 0.1 M $HClO_4$ [161107_225030]

This result looks similar to the same substrate when it has been etched more aggressively. For optimization of the sample cleaning procedure, etching had been performed at higher temperatures than the 65 °C used for sample preparation for this thesis. The results obtained when etching at 80 °C also exhibit small roughly rectangular terraces as observed in figure 5.11. The radicals on the surface may change the way the surface interacts with the piranha solution, hindering the etching of a nicely uniform surface with large terraces. For comparison, figure 5.12 shows the surface scanned with AFM, in air, before and after the grafting experiments.

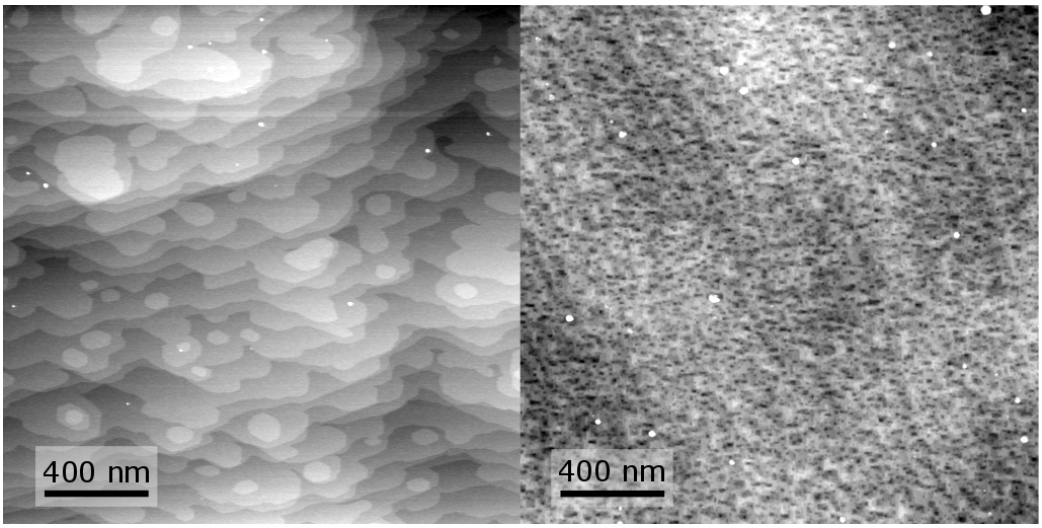

Figure 5.12: AFM images of rutile TiO_2(110) before (left, [161013_114033]) and after grafting experiments (right, [161108_171818])

6 Conclusion

The electrochemical STM was improved in order be able to reliably produce atomic resolution on oxide samples.

Instead of the previously used platinum quasi reference electrode, a palladium-hydrogen reference electrode now provides a stable and well-defined reference potential. Oxygen can be removed from the system, which eliminates additional processes from *in situ* measured electrochemistry, provides clearer STM images, and opens a larger range of bias voltages available for scanning. Platinum-iridium tips are now used instead of tungsten tips, avoiding the contamination of the sample through the measurement.

The obtained STM images show what the electrochemical STM can do as it is now, and pave the way for further studies of oxides under ambient conditions.

Appendix

List of Figures

References

[1] Wiechers J., Twomey T., Behm R. and Kolb D., *An in-situ scanning tunneling microscopy study of Au(111) with atomic scale resolution*: Journal of Electroanalytical Chemistry, 248:451–460 (1988)

[2] Itaya K. and Tomita E., *Scanning tunneling microscope for electrochemistry - a new concept for the in situ scanning tunneling microscope in electrolyte solutions*: Surface Science Letters, 201 (1988)

[3] Diebold U., *The surface science of titanium dioxide*: Surface Science Reports, 48:53–229 (2003)

[4] Henderson M., *A surface science perspective on TiO_2 photocatalysis*: Surface Science Reports, 66:185–297 (2011)

[5] ORegan B. and Grätzel M., *A low-cost, high efficiency solar cell based on dye-sensitized colloidal TiO_2 films*: Nature, 353:737–740 (1991)

[6] Kavan L., Grätzel M., Gilbert S., Klemenz C. and Scheel H., *Electrochemical and Photoelectrochemical Investigation of Single-Crystal Anatase*: Journal of the American Chemical Society, 118:6716–6723 (1996)

[7] Li M., Hebenstreit W., Diebold U., Tyryshkin A.M., Bowman M.K., Dunham G.G. and Henderson M.A., *The Influence of the Bulk Reduction State on the Surface Structure and Morphology of Rutile TiO2(110) Single Crystals*: Journal of Physical Chemistry B, 104:4944–4950 (2000)

[8] Diebold U., Li S.C. and Schmid M., *Oxide Surface Science*: Annual Review of Physical Chemistry, 61:129–148 (2010)

[9] Schmid M., *Experimentelle Methoden der Oberflächenphysik* (2011), lecture notes

[10] Choi J.I.J., Mayr-Schmölzer W., Mittendorfer F., Redinger J., Diebold U. and Schmid M., *The growth of ultra-thin zirconia films on $Pd_3Zr(0001)$*: Journal of Physics: Condensed Matter (1984)

[11] Song A., Jing D. and Hines M.A., *Rutile Surface Reactivity Provides Insight into the Structure-Directing Role of Peroxide in TiO_2 Polymorph Control*: Journal of Physical Chemistry C, 118:27343–27352 (2014)

[12] Gritzer G. and Kuta J., *Recommendations on Reporting Electrode Potentials in Nonaqueous Solvents*: Pure and Applied Chemistry, 56:461–466 (1984)

[13] Vasile M.J. and Enke C., *The preparation and therodynamic properties of a Palladium-Hydrogen Electrode*: Journal of the Electrochemical Society (1965)

[14] Lukaszewski M. and Czerwinski A., *The method of limited volume electrodes as a tool for hydrogen electrosorption studies in palladium and its alloys*: Journal of Solid State Electrochemistry, 15:2489–2522 (2011)

[15] Chandra D., Reilly J.J. and Chellappa R., *Metal Hydrides for Vehicular Applications: The State of the Art*: JOM, 58:26–32 (2006)

[16] Schuldiner S., Castellan G.W. and Hoare J.P., *Electrochemical Behaviour of the Palladium-Hydrogen System. I. Potential-Determining Mechanisms*: The Journal of Chemical Physics, 28:16–19 (1958)

[17] Bard A.J. and Faulkner L.R., *Electrochemical Methods: Fundametals and Applications*: Wiley, 2nd edition (2001)

[18] Schuldiner S. and Hoare J.P., *Note on the potential of the α- Pd/H2 Electrode*: The Journal of Chemical Physics, 23:1551 (1955)

[19] Zhang J. and Ulstrup J., *Oxygen-free In Situ Scanning Tunnelling Microscopy*: Journal of Electroanalytical Chemistry, 599:213–220 (2007)

[20] Cussler E.R., *Diffusion - Mass Transfer in Fluid Systems*: Cambridge University Press, 3rd edition (1997)

[21] Lide D.R., editor, *CRC Handbook of Chemistry and Physics*: CRC Press, 78th edition (1997)

[22] Andoralov V.M., Tarasevich M.R. and Tripachev O.V., *Oxygen reduction reaction on polycrystalline gold. Pathways of hydrogen peroxide transformation in the acidic medium*: Russian Journal of Electrochemistry, 1327 (2011)

[23] Mertens S.F., Gara M., Sologubenko A.S., Mayer J., Szidat S., Krämer K.W., Jacob T., Schiffrin D.J. and Wandlowski T., *Au Hg Nanoalloy Formation Through Direct Amalgamation: Structural, Spectroscopic, and Computational Evidence for Slow Nanoscale Diffusion*: Advanced Functional Materials, 9:3259–3267 (2011)

[24] Müllner M., Balajka J., Schmid M., Diebold U. and Mertens S.F., *Self-limiting adsorption of WO3 oligomers on oxide substrates in solution: The case against using W-tips in electrochemical STM*: Nano Letters (2017), submitted

[25] Renner A., *Preparation of Platinum/Iridium Tips for Scanning Tunnelling Microscopy with KOH/KSCN Solution* (2014), project work

[26] Goh C., Scully S.R. and McGehee M.D., *Effects of molecular interface modification in hybrid organic-inorganic photovoltaic cells*: Journal of Applied Physics, 101 (2007)

[27] Campbell W.M., Burrell A.K., Officer D.L. and Jolley K.W., *Porphyrins as light harvesters in the dye-sensitised TiO_2 solar cell*: Coordination Chemistry Reviews, 248:1363–1397 (2004)

[28] Guo Q., Cocks I. and Williams E., *The adsorption of benzoic acid on a TiO_2(110) surface studied using STM, ESDIAD and LEED*: Surface Science, 393 (1997)

[29] Guo Q. and Williams E., *The effect of adsorbate-adsorbate interaction on the structure of chemisorbed overlayers on TiO_2(110)*: Surface Science, 433-435:322–326 (1999)

[30] Skibinski E.S., Song A., DeBenedetti W.J.I., Ortoll-Bloch A.G. and Hines M.A., *Solution Deposition of Self-Assembled Benzoate Monolayers on Rutile (110): Effect of π - π Interactions on Monolayer Structure*: Journal of Physical Chemistry C, 120:11581–11589 (2016)

[31] Greenwood J., Phan T.H., Fujita Y., Li Z., Ivasenko O., Vanderlinden W., Gorp H.V., Frederickx W., Lu G., Tahara K., Tobe Y., Uji-i H., Mertens S.F.L. and Feyter S.D., *Covalent Modification of Graphene and Graphite Using Diazonium Chemistry: Tunable Grafting and Nanomanipulation*: ACS Nano, 9:5520–5535 (2015)

[32] Merson A., Dittrich T., Zidon Y., Rappich J. and Shapira Y., *Charge Transfer from TiO_2 into adsorbed benzene diazonium compounds*: Applied Physics Letters, 85 (2004)